Cement and Concrete Research 140 (2021) 106287

Contents lists available at ScienceDirect

Cement and Concrete Research

journal homepage: www.elsevier.com/locate/cemconres

Iron speciation in blast furnace slag cements

A. Mancini [a,b], B. Lothenbach [c,d,*], G. Geng [a,e], D. Grolimund [f], D.F. Sanchez [f], S.C. Fakra [g], R. Dähn [a], B. Wehrli [b], E. Wieland [a]

[a] Paul Scherrer Institut, Laboratory for Waste Management, 5232 Villigen PSI, Switzerland
[b] ETH Zurich, Institute of Biogeochemistry and Pollutant Dynamics, 8092 Zurich, Switzerland
[c] Empa, Laboratory for Concrete & Construction Chemistry, 8600 Dübendorf, Switzerland
[d] NTNU, Department of Structural Engineering, Trondheim, Norway
[e] National University of Singapore, Department of Civil and Environmental Engineering, 117576, Singapore
[f] Paul Scherrer Institut, Swiss Light Source, 5232 Villigen PSI, Switzerland
[g] Lawrence Berkeley National Laboratory, Advanced Light Source, Berkeley, CA 94720, USA

ARTICLE INFO

Keywords:
Slag
Iron
Corrosion
XAS
Thermodynamic model

ABSTRACT

Slag-containing pastes and concretes were analysed by element-specific synchrotron-based techniques to determine the speciation of iron on crushed materials through spatially resolved micro-spectroscopic studies. The investigated cement samples were hydrated either in the laboratory, or exposed to river or sea water. Metallic iron, along with minor proportions of iron sulphide and magnetite was detected in the laboratory sample. Iron sulphide, goethite, and siliceous hydrogarnet were discovered in the blended slag cements hydrated in contact with river water for up to 7 years. In contrast, no Fe(0) was observed in blended concretes exposed to sea water. Instead, iron sulphide, iron(II)-hydroxide and -oxide, hematite, magnetite, siliceous hydrogarnet, and goethite were detected as well as ilmenite ($FeTiO_3$) in the aggregates. The strong acceleration of Fe oxidation in samples exposed to sea water and the long-term passivation observed in the other samples indicate comparable processes as those occurring on steel bars.

1. Introduction

Cement-based building materials play a key role in modern infrastructures and housing because of their low cost, high performance and availability of the raw materials. Due to increasing production, however, cement manufacture contributes to 8% of global anthropogenic CO_2 emission [1]. The replacement of a part of the cement clinker by inorganic supplementary cementitious materials, such as pozzolans, calcined clays or industrial by-products (fly ash or ground granulated blast furnace slag, GGBFS) is an efficient method to reduce these CO_2 emissions [2].

GGBFS is a by-product of iron- and steel-production from the reduction of iron ore to pig iron in the blast furnace [3]. The liquid slag is rapidly cooled to form granules, which are then ground to a fineness similar to Portland clinker. In 2018, 15 Mt. GGBFS were produced worldwide [4]. GGBFS has a high content of CaO, Al_2O_3 and MgO, which makes it an ideal replacement for clinker in the cement production. GGBFS also contains a substantial amount of Fe(0) (~1–5 weight (wt%) in terms of Fe_2O_3), which is present as finely dispersed metallic nano- to micron-sized particles [5]. It has been observed that those Fe(0) particles were not oxidised and thus stable for at least 28 days in alkali activated slag hydrated under laboratory conditions [5]. At present, the long-term fate of Fe(0) in alkali-activated slags as well as the behaviour of Fe(0) in blends with Portland cements (PC) and in samples exposed to different environment is unknown. In particular, it is unclear at what rate and to what extent Fe(0) corrodes and the nature of the corrosion products formed.

It can be expected that the corrosion behaviour of Fe(0) in slag-containing cements could be similar to that of iron (and steel) reinforcing bars in concrete structures, although the kinetics might be different due to the large surface area of the micron-sized granules and the presence of reducing conditions in the pore solution [6,7]. The corrosion of reinforcing bars in concrete has been extensively investigated in the last decades [e.g. 8–10]. These studies show that the corrosion rate is mainly controlled by the chemical conditions (i.e. pH, redox conditions, elemental composition of cement pore water, etc.) and that a variety of Fe-containing corrosion products are formed. Furthermore, the spontaneous corrosion of steel forms a passive protecting thin

* Corresponding author at: Laboratory for Concrete & Construction Chemistry, 8600 Dübendorf, Switzerland.
E-mail address: barbara.lothenbach@empa.ch (B. Lothenbach).

https://doi.org/10.1016/j.cemconres.2020.106287
Received 11 June 2020; Received in revised form 9 September 2020; Accepted 26 October 2020

film on ordinary reinforcing steel embedded in an alkaline pore solution [11,12].

The kind of corrosion products formed has been investigated mainly in ancient archaeological samples that have undergone atmospheric (oxic) corrosion in natural environments over long periods of time (for example [13,14]). Under atmospheric conditions, goethite (α-FeOOH), lepidocrocite (γ-FeOOH), and magnetite/maghemite (Fe_3O_4, γ-Fe_2O_3) were found to be the main corrosion products [9,15–21]. Minor portions of siderite ($FeCO_3$) and Fe-chlorides ($Fe_2(OH)_3Cl$, β-FeO(OH,Cl)) were also reported [9,16,22,23]. These findings are in agreement with laboratory experiments of iron corrosion under oxic conditions [24,25] and investigations of steel bars embedded in concrete for 65 years [26]. One of the major issues of the formation of such Fe corrosion products within concrete is the significant volume difference between Fe(0) and corrosion products (Fig. 1), which leads to expansion and cracking of the concrete.

Limited literature is available on anaerobic corrosion of steel in concrete. Anaerobic conditions can arise, for example, in water saturated soils or sediments and they can be replicated in a glove box with inert N_2 atmosphere in laboratory studies. The iron corrosion products produced by anaerobic corrosion are magnetite (Fe_3O_4) [27,28] and "black rust", which is mainly composed of magnetite as well [29,30]. Also siliceous hydrogarnet, the main Fe-containing phase in hydrated Portland cement paste [31,32], has recently been identified as oxidation product of steel in cements [28]. Studies carried out on archaeological samples buried in soil containing carbonates [22,33–35] described the presence of Fe-carbonate phases (such as siderite and chukanovite) and/or magnetite, depending on pH and carbonate concentration. The presence of reduced sulphur species in slag cements indicates that strongly reducing conditions prevail, and iron is expected to precipitate as iron sulphide [36,37].

In addition to the formation of corrosion products, it is anticipated that Fe(II,III) species generated during the course of Fe(0) corrosion may also interact with cement phases present at the interface between steel and cement paste. It has been reported that Fe(III) can substitute Al(III) in Al-containing cement phases, such as ettringite ($Ca_6(Al,Fe)_2(SO_4)_3(OH)_{12}\cdot 26H_2O$) and AFm phases (Al-Fe-mono phase such as monosulphate: $Ca_4(Al,Fe)_2SO_4(OH)_{12}\cdot 6H_2O$) [32,42–44], and that Fe(III) can be sorbed by C-S-H (calcium silicate hydrate) phases [45]. In Portland cements, Fe/Al siliceous hydrogarnet was identified as the thermodynamically stable Fe(III)-bearing phase [31,32]. Much less is known on the interaction of Fe(II) with cement phases. Recently it was shown

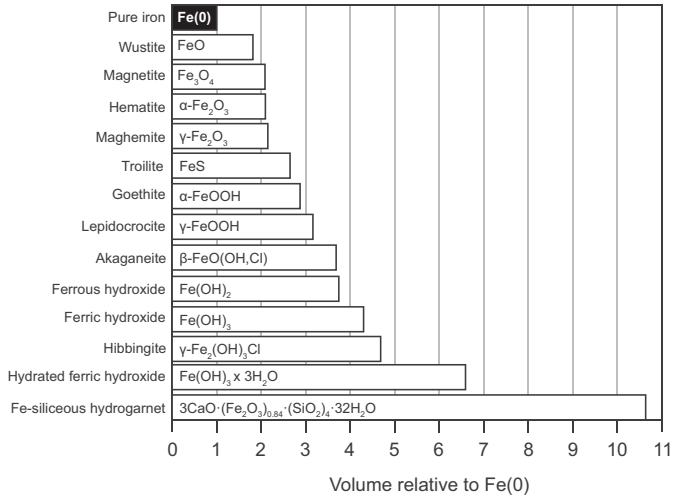

Fig. 1. Relative volumes of possible corrosion products as compared to pristine Fe(0) (molar volume of Fe(0) = 7.1 cm^3/mol [38]). Figure and data modified from [39,40], data for troilite, akaganeite, and hibbingite from [41] and for siliceous hydrogarnet from [32].

that Fe(II) can also be taken up by C-S-H phases and possibly also, to a lower extent, by AFm phases [46].

Synchrotron radiation-based spectroscopic techniques are powerful tools for investigating the chemical form of a specific element inside complex matrices. X-ray absorption spectroscopy (XAS) has previously provided element-specific structural information at different scales in cement systems [47–50] and in particular on the coordination environment of Fe in cement matrices [42,43]. XAS allows Fe-containing phases in cement matrices to be distinguished from their Al-analogues, which cannot be achieved by standard techniques such as laboratory X-ray diffraction (XRD) or thermogravimetric analysis (TGA), due to a strong overlap of the signals [42]. In addition, Fe species are often present in amorphous form and at low concentrations, which are not detectable by standard analytical techniques. Synchrotron radiation-based X-ray fluorescence can be applied at the micro-scale (micro-XRF) to discern the two-dimensional distribution of the elements (elemental mapping). In particular, the acquisition of several XRF maps recorded at specific energies around the absorption edge allows discerning the distribution of the redox species for the element of interest [51,52]. Hence, synchrotron radiation-based spectroscopic techniques are well suited for investigating the Fe speciation in cementitious systems.

In this study the corrosion of Fe(0) present in slag-containing cements was explored by using standard analytical techniques in combination with synchrotron-based techniques and thermodynamic modelling. The slag cements had been exposed to different aqueous conditions with exposure times ranging from 6 to 34 years. The samples were investigated with the aim of characterising and quantifying the Fe-containing corrosion products resulting from the corrosion of pristine Fe (0) in the slag-containing cements.

2. Experimental

2.1. Slag samples and bulk analyses

Four slag cement samples aged under different environmental conditions were investigated in this study. These samples represent three different ageing environments, i.e. laboratory conditions and samples exposed to sea water and river water:

- The sample "*Lab*" denotes a supersulphated slag cement hydrated for 6 years in closed PE vessels at 20 °C. The slag cement consisted of 84.5 wt% slags, of 15 wt% anhydrite and 0.5 wt% KOH prepared at a water/binder (w/b) ratio of 0.4 following the mixes outlined by Gruskovnjak et al. [36].
- A CEM III/B 42.5 N (containing ~70 wt% slag) from the trial site of the Femern Belt between Denmark and Germany as described in Jakobsen et al. [10]. This set includes the non-hydrated initial cement (labelled *Fem*), the same cement hydrated for 28 days at water/cement (w/c) ratio = 0.5 at 20 °C in closed polyethylene (PE) vessels in the laboratory (*Fem_reac*), and two casted concrete samples (CEM III/B) exposed to sea water conditions below the tidal level for 2 (*Fem_sea_2y*) and 5 years (*Fem_sea_5y*), respectively (w/c = 0.4; cement/(aggregate + sand) = 0.19).
- The concrete "*River*" is the near-surface part of a drill core from the cantilever of a bridge located in the village Auw an der Kyll in Germany and exposed for 7 years to river water, without obvious cracks. The cement is reported to be a CEM III/A 42.5 N, w/c = 0.5, and containing 35–63 wt% Portland cement and 36–65 wt% slag.
- The "*Seawater*" concrete is the near surface part of a drill core with no obvious cracks, sampled from a pillar of the "Vejle Fjord bridge" in Denmark, which has been exposed to marine conditions below the water level [10]. The bridge was built in 1974 and the sampling occurred in 2008, and hence this is the oldest investigated sample (34 years old). The concrete was based on a CEM III/B 42.5 N

(containing ~71 wt% slag), w/c = 0.45, cement/(aggregate + sand) = 0.22 [53,54].

The chemical composition of the samples *Lab*, *Fem*, *River*, and *Seawater* were determined by laboratory X-ray fluorescence (XRF) and the C content by combustion analysis according to DIN ISO 10694. The measured compositions of the samples *River* and *Seawater* were corrected for the presence of sand and aggregate as detailed in Table 1. The unhydrated and hydrated samples *Lab*, *Fem_reac*, *River*, and *Seawater* were also characterized by laboratory X-ray diffraction (XRD), and thermogravimetric analysis (TGA). The XRD patterns were recorded on a PANalytical X'Pert Pro MDF diffractometer using CoKα radiation and an X'Celerator detector. Diffraction patterns were collected from 5° to 70° 2θ at a step size of 0.017° 2θ. TGA data were recorded with a Netzsch STA 449 Jupiter device using approximately 30 mg of sample. The weight loss was recorded on powder samples from 30° to 980 °C at a heating rate of 20 °C/min under N_2 atmosphere.

Thin sections (~30 μm) of the hydrated samples *Lab*, *River*, and *Seawater* were prepared and coated with carbon for morphological investigations by scanning electron microscope (SEM) using a FEI Quanta 650. The backscattered electron (SEM-BSE) mode was used at an acceleration voltage of 12 kV and a pressure of 3.0–5.0 × 10^{-6} Torr. Electron diffraction analysis (SEM-EDX) was performed with a Thermo Noran Ultra Dry 60 mm^2 detector and Pathfinder X-Ray Microanalysis Software.

2.2. Thermodynamic modelling

The hydrate compositions of the *Seawater* and *River* samples in contact with sea water and fresh water, respectively, were thermodynamically modelled using the geochemical modelling code Gibbs Energy Minimization Selektor (GEMS) [56]. GEMS computes equilibrium phase assemblages and speciation in complex geochemical systems. The general thermodynamic data were selected from the PSI/Nagra thermodynamic database [57,58], complemented with solubility products of the cement phases from [59]. The C-S-H phase was modelled using the "CNASH" model from Myers et al. [60], which accounts for the uptake of alkali and aluminium in the C-S-H phase. The uptake of Fe(II) and Fe(III) by C-S-H was calculated using a K_d value of 700 m^3/kg for Fe(III) [45] and of 0.1 m^3/kg for Fe(II) [46]. The K_d distribution coefficients account for the capacity of C-S-H to take up Fe(II,III). Thermodynamic data for akaganeite (β-FeO(OH,Cl)), hibbingite ($Fe_2(OH)_3Cl$), and greenrust (GR (SO_4^{2-}, Cl^-, CO_3^{2-})) were added [61–63]. The formation of quartz (SiO_2), dolomite ($CaMg(CO_3)_2$), pyrite (FeS_2), goethite (FeOOH), and hematite (Fe_2O_3) in the hydrated cements was suppressed in the calculations due to kinetic reasons. The consideration of hematite and goethite would supress the formation of siliceous hydrogarnet ($(CaO)_3(Al,Fe)_2O_3(SiO_2)_{0.84}(H_2O)_{4.32}$) in the calculation as shown elsewhere [32].

The composition of the cements as determined by XRF (Table 1) and the average compositions of both sea water and river water were used (see Table S1 in Supplementary information (SI) for compositions) to calculate the composition of the hydrated cements. For the *Fem_reac* cement an additional calculation was carried out assuming a reaction degree of the slag of 33% [7] in order to account for the limited degree of slag reaction after the relatively short reaction time of 28 days. For this calculation, performed at a lower degree of slag reaction, the oxide composition as given in Table S2 in SI was used, considering 70% slag and 30% Portland cement in the CEM III/B.

Table 1
Oxide composition (g/100 g) of the investigated samples measured with XRF[a].

	Lab	*Fem*	*River*	*Seawater*
	Unhydrated	Unhydrated	Hydrated	Hydrated
	SSC[b]	CEM III/B 42.5[c]	CEM III/A 42.5 N[d]	CEM III/B 42.5 N[e]
	g/100 g	*g/100 g*	*g/100 g*	*g/100 g*
CaO	36.0	48.4	44.0	49.8
SiO_2	38.2	30.6	31.5	28.9
Al_2O_3	14.1	9.4	8.4	10.6
Fe_2O_3	1.4	0.9	2.0	1.3
MgO	6.6	4.8	3.4	4.5
Na_2O	0.5	0.2	0.6	0.3
K_2O	0.6	0.7	0.9	0.5
TiO_2	0.5	0.9	0.7	n.a.
Mn_2O_3	1.0	0.2	0.6	n.a.
P_2O_5	0.0	0.2	0.6	n.a.
SO_3	1.2	3.9	3.2	2.7
CO_2	n.a.	0.7	2.9	1.2
LOI	−0.5	−0.5	5.24	1.4

[a] The content of some minor elements such as Cl, F was not analysed.
[b] SSC contains 15% $CaSO_4$ and 0.5% KOH; slag composition also reported in Ben Haha et al. [55].
[c] CEM III/B 42.5: Portland cement: ≈33%, slag: ≈67%, CEM III/B composition reported in Jakobsen et al. [10]: 48% CaO %, 30% SiO_2, 9.4% Al_2O_3, 0.7% Fe_2O_3, 4.9% MgO and 2.5% SO_3.
[d] CEM III/A 42.5 N: Portland cement: 35–63%, slag: 36–65%; the measured XRF composition was corrected for the presence of sand and aggregate (cement/(aggregate + sand) = 0.18) assuming that they were composed of SiO_2 (quartz).
[e] CEM III/B 42.5: Portland cement: 29%, slag: 71% [53,54].

2.3. Synchrotron radiation-based spectroscopy

In addition to XRD and TGA the Fe-containing phases in cement matrices were also studied with XAS, which allows determination of the iron speciation in the complex cement matrices. Two of the most frequently used synchrotron-based techniques are micro X-ray fluorescence (micro-XRF) and bulk/micro X-ray absorption near edge structure (XANES) spectroscopy. In this study, Fe K-edge XANES was used to identify Fe-bearing compounds and the oxidation products of Fe(0) in the cementitious matrices, while XRF mapping carried out at specific energies was used to generate Fe redox maps.

2.3.1. Bulk-XANES data collection

Fe K-edge XANES data of the bulk samples (in powder form) and most Fe references were acquired at the Dutch-Belgian beamline (Dubble - European Synchrotron Radiation Facility (ESRF), Grenoble, France) and at the Samba beamline (Soleil, Saint Aubin, France). Both beamlines are equipped with a Si(111) monochromator and the energy was calibrated at the Fe K-edge (7112 eV) using an iron foil. All measurements were performed at room temperature and the spectra were collected in fluorescence mode by a 9-element monolithic detector (Dubble) or by a Canberra 35-elements monolithic planar Ge pixel array (Samba). For each sample, several spectra were acquired and merged. Fe reference samples were prepared by mixing the Fe-containing compounds (Fe(II, III)-loaded cement phases, commercially available Fe minerals and chemicals) with boron nitride (BN) to attenuate the absorption intensity [64,65] (Fig. 2). The collected spectra were processed using the ATHENA software package (Demeter version 0.9.26) according to procedures described elsewhere [66]. Pre-edge background subtraction and normalisation were carried out by fitting a first-degree polynomial to the pre-edge and a third-degree polynomial to the post-edge regions of the adsorption spectra. After standard background subtraction and normalisation, corrections for the edge position were carried out. To this end, a Fe-siliceous hydrogarnet (Fe-Si-Hyd) sample was measured at the different beamlines and used as a reference for adjusting the edge position. During data processing with Athena, the spectra were aligned to a common energy scale setting the first inflection point of the first derivative of this reference to 7126.3 eV (energy at the half step-size) in Athena. Subsequently, the experimental spectra of the measured samples were corrected according to the observed shift in the absorption energy.

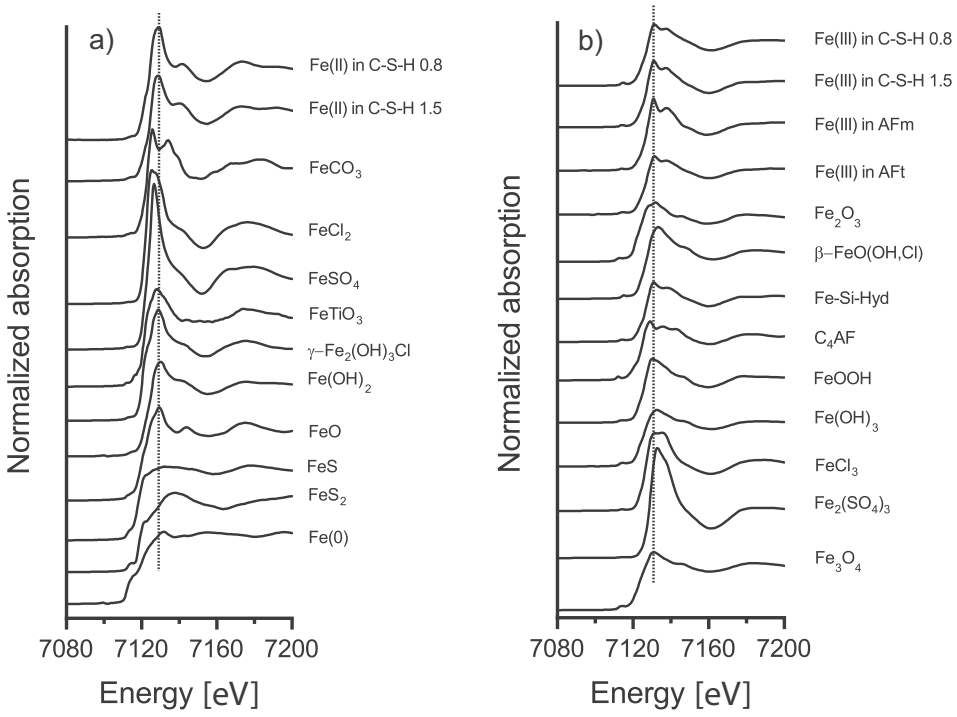

Fig. 2. Fe K-edge XANES spectra of the references used for linear combination fitting. a) Fe(0) and Fe(II) references, b) magnetite (Fe_3O_4) and Fe (III) references. Fe(0) = metallic iron, FeS_2 = pyrite, FeS = mackinawite, FeO = Fe(II) oxide, Fe_2O_3 = hematite, $Fe(OH)_2$ = Fe(II) hydroxide, γ-$Fe_2(OH)_3Cl$ = hibbingite, $FeTiO_3$ = ilmenite, $FeSO_4$ = iron(II) sulphate, $FeCl_2$ = Fe(II) chloride, $FeCO_3$ = siderite, Fe_3O_4 = magnetite, $Fe_2(SO_4)_3$ = Fe(III) sulphate, $FeCl_3$ = Fe(III) chloride, $Fe(OH)_3$ = Fe(III) hydroxide, FeOOH = goethite, C_4AF = ferrite clinker, Fe-Si-Hyd = iron siliceous hydrogarnet, and β-FeO(OH,Cl) = akaganeite. Vertical lines indicate the white line position of a) Fe(II) (FeO: 7129.3 eV) and b) Fe(III) (Fe-siliceous hydrogarnet: 7131.2 eV).

2.3.2. *Micro-XRF and micro-XANES*

Two-dimensional micro-XRF redox maps and micro-XANES spectra were recorded on the microXAS beamline of the Swiss Light Source (SLS), Villigen, Switzerland [67], and on the XFM beamline 10.3.2 of the Advanced Light Source (ALS), Berkeley, USA [68]. Both beamlines are equipped with Si(111) crystal monochromators and at both beamlines, the two-dimensional XRF redox maps were collected using *x-y* scanning stages. All data were recorded at room temperature in fluorescence mode. The same thin sections as used for SEM analyses were mounted at a 45° angle to the incident beam and exposed to monochromatic X-ray radiation of variable energy at a spot size of ~1.5 × 1.5 μm^2 at the SLS and ~2.0 × 2.5 μm^2 at the ALS. The energies were selected to achieve an optimal chemical contrast based on Fe(0), Fe(II), and Fe(III) reference spectra (Fig. 3). Fluorescence emission was monitored with a Ketek one element silicon drift detector SDD (SLS) or a Canberra 7 elements SDD detector (ALS), respectively.

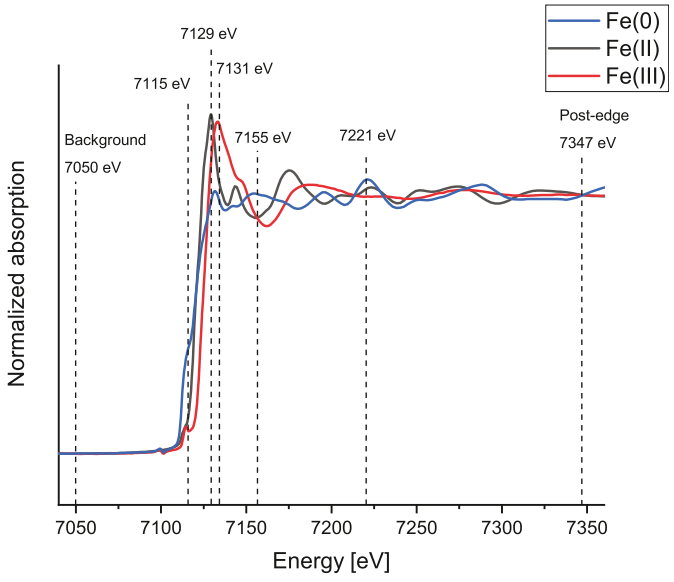

Fig. 3. Experimental XAS spectra of Fe(II), Fe(III) and Fe(0) reference compounds. Micro-XRF maps were recorded at the indicated energies resulting in the highest chemical contrast between the three Fe redox states.

Micro-XANES spectra were collected at the Fe K-edge (7112 eV [69] at SLS and 7110.75 eV [70] at 10.3.2) on locations of interest on the micro-XRF maps of the thin sections. The monochromator angle was calibrated by assigning the energy of 7112 eV (at SLS) or 7110.75 eV (at ALS 10.3.2) to the first inflection point of the Fe K-edge spectrum of an iron metallic foil. At least four spectra were acquired at each point of interest. Processing of micro XANES data was performed as described for the bulk data.

2.3.3. *Micro-XRD*

Micro-XRD measurements were performed at the microXAS beamline of the SLS. The incident beam energy was set to 14.6 keV and focused to a spot size ~1.5 × 1.5 μm^2 using Kirkpatrick-Baez mirrors. A one element Ketek SDD was placed near the sample to record the fluorescence signal. An Eiger 4M area detector was placed at the downstream side of the sample to collect the diffraction pattern of the scanned region in transmission mode. The sample-to-plate distance and the position of the beam centre were calibrated by the diffraction pattern of a standard material (LaB_6). The probed 2theta spacing range was 8.6 Å (low angle) to 0.95 Å (high angle). A sub region (approximately 3 × 3 mm) rich in Fe was scanned at a spatial resolution of 10 μm × 10 μm. The raw 2D diffraction patterns were processed diffractograms by our own Python codes coupled with *ImageJ* [71]. The identification of the crystalline phase structures was performed using a commercial software (HighScore Plus).

2.3.4. *Data analyses*

2.3.4.1. XANES. The least-square linear combination (LC) fitting as implemented in the IFEFFIT software package (ATHENA) was carried out to determine the contribution of the XANES spectrum of a reference compound to the experimental XANES spectra of the unknown mixture [66]. The coefficients were normalized to 1, meaning that each spectral contribution ranges from 0 (not present) to 1 (dominant species). Prior

to LC fitting, principal component analysis (PCA) and iterative target-transformation (TT) were performed with the aim of determining the minimal amount of independent components needed to reproduce an experimental spectrum (PCA) and of identifying the reference compounds needed to reconstruct the experimental spectrum [72]. The so-called SPOIL number was proposed as indicator for the probability that a reference spectrum contributes to the experimental spectra [72]. It is a non-negative dimensionless number for which values of 0–3 are indicating high probability, and >3 reflect low probability, respectively [72]. The PCA tools included in Athena [66], Sixpack [73], and the 10.3.2 LabVIEW custom software [68] were used for PCA and TT. The spectra of the slag cements were reproduced as the sum of different single Fe reference compounds.

2.3.4.2. Chemical speciation maps. Normalized Fe K-edge XANES spectra provide information on the chemical speciation of the absorber atom, for example in case of the three reference compounds having different oxidation states, i.e. metallic iron for Fe(0), FeO for Fe(II) and $Fe(OH)_3$ for Fe(III), shown in Fig. 3. The differences in chemical contrast were used to record two-dimensional distribution maps of the Fe oxidation states in the samples [52]. X-ray fluorescence maps of the areas of interest were recorded by tuning the excitation energy to the selected energies with the highest chemical contrast for the three Fe species (7115 eV (Fe(0)), 7129 eV (Fe(II)), 7131 eV (Fe(III)), 7155 and 7221 eV (Fe(0))) and normalized to those recorded at 7050 eV (zero, pre-edge) and 7347 eV (one, post-edge). The absorption coefficients of each Fe species were taken from the normalized spectra of the reference minerals (Fig. 3). The percentage of each Fe species at each scanned pixel was determined by applying a least-square fitting procedure to the absorption intensities in the five maps collected at 7115 eV, 7129, 7131, 7155 and 7221 eV.

3. Results

3.1. Hydrated slag samples

3.1.1. Solid phases

The investigated samples have been hydrated in different environmental conditions and a first macroscopic investigation by using standard analytical techniques, such as laboratory XRD and TGA, allowed to identify the main differences in the hydrates formed (Fig. 4). Ettringite, C-S-H, hydrotalcite ($Mg_6Al_2(OH)_6CO_3{\cdot}8H_2O$) were present in all samples, in addition to carbonate phases (calcite, vaterite and dolomite) which, however, were not present in the *Lab* sample. Due to the high calcium sulphate content, ettringite and gypsum were, in addition to C-S-H, the dominant phases in the *Lab* sample. Some gypsum signal was possibly also present in the *Seawater* sample. The AFm phases were present as hemicarbonate ($Ca_4Al_2(OH)_{12}(CO_3)_{0.5}{\cdot}5.5H_2O$) in *Fem_reac*, monocarbonate ($Ca_4Al_2(OH)_{12}CO_3{\cdot}5H_2O$) in *River*, *Seawater* and possibly *Fem_reac*, as well as monosulphate ($Ca_4Al_2(OH)_{12}SO_4{\cdot}6H_2O$) and possibly Friedel's salt (Cl-rich AFm – $Ca_2Al(OH)_6Cl{\cdot}2H_2O$) in the *Seawater* sample. Friedel's salt was identified mainly by its typical weight loss in TGA, while unbiased identification by XRD was difficult due to its small quantity and the broadening of its basal reflection. Portlandite ($Ca(OH)_2$) was observed in *Seawater* and *Fem_reac*, while it was absent in the *River* and *Lab* samples, which contained less CaO. The two concrete samples (*Seawater* and *River*) showed in addition strong peaks caused by the presence of quartz and from other aggregates. The aggregates present in the *Seawater* sample contained in addition some sheet silicates at low 2theta angle in addition to feldspar and ilmenite ($FeTiO_3$).

3.1.2. Hydrate composition calculated by thermodynamic modelling

For comparison, thermodynamic modelling was performed to calculate the expected composition of the investigated samples (Fig. 5). The compositional data listed in Table 1 were used for the modelling by assuming a complete reaction of both the Portland cement and the slag. A hydrate assemblage consisting of hydrotalcite, C-S-H, ettringite, zeolites as well as FeS and Fe_3O_4 was calculated for the *Lab* sample, which contained only slag but no Portland cement and thus relatively little CaO. The calculated phase composition agrees with the experimental observations in this type of supersulphated slags [36]. Presence of gypsum was not predicted as slag was assumed to completely react.

Al-containing hydrotalcite, C-S-H, monocarbonate, ettringite, FeS, and Fe_3O_4 were also predicted to be present in the three blended PC-slag samples *Fem_reac*, *River* and *Seawater*. In addition, hemicarbonate was predicted for the *Fem_reac* and *Seawater* samples, while presence of calcite and strätlingite ($Ca_2Al_2SiO_2(OH)_{10}{\cdot}3H_2O$) was predicted for the *River* sample. An additional calculation was carried out for the *Fem_reac* cement by assuming a reaction degree of the slag of only 40% (e.g. *Fem_reac_40*) in order to account for the limited degree of slag reaction after the relatively short reaction time of 28 days [7]. For the *Fem_reac_40* sample the presence of some portlandite instead of strätlingite was predicted, in addition to C-S-H, ettringite, monocarbonate, Al-containing hydrotalcite, and siliceous hydrogarnet (as Fe-rich phase); in no case Fe-containing AFm, AFt or hydrotalcite-like phases were predicted. The absence of portlandite in the calculated phase assemblage of *River* and *Seawater* seems to be related to the assumption of complete slag reaction. In general, the calculated compositions of the *Lab*, *River* and *Fem_reac* samples are in good agreement with the observed XRD and TGA data described in Section 3.1.1. The presence of Friedel's salt and a minor amount of gypsum in the *Seawater* sample shown in Fig. 4 is considered to be due to the interaction with chloride and sulphate present in the water, as discussed in the following section.

3.1.3. Predicted chemical changes caused by exposure to river or sea water

The effect of the interaction of the hydrated cements with river and sea water was also thermodynamically modelled (Fig. 6a-f). The left hand side of the composition of the hydrated cements corresponds to that shown in Fig. 5. To the right the gradual changes towards the surface of the concretes exposed to either river or sea water are displayed. The vicinity of the concretes to the river or sea water was simulated by increasing the amount of exposure solutions (for details see [74,75]).

For the *River* sample (Fig. 6a/c/e), C-S-H phases, ettringite, strätlingite, monocarbonate, hydrotalcite, and calcite were calculated to exist in the non-exposed zone at an initial pH of 13.7. The formation of calcite (from the carbonate contained in the river water) and of thaumasite ($Ca_3(SiO_3)(CO_3)(SO_4){\cdot}15H_2O$) in all samples was predicted closer to the surface, while the pH was calculated to drop to pH 12. At the surface of the concrete, where more intense exposure to river water occurs, the formation of M-S-H phases and zeolites was predicted, while C-S-H was destabilized and the pH value dropped to 11. Magnetite (Fe_3O_4) and troilite (FeS) were predicted as the Fe compounds in the non-exposed cement, and the E_h of −650 mV indicates strongly reducing conditions. The formation of $Fe(OH)_3$ instead of magnetite and troilite was predicted at the surface of concrete, i.e. at a more intense exposure to river water, coinciding with an increase in E_h towards more oxidizing conditions. Very low Fe concentrations of 0.01 μmol/L and below were calculated resulting in very low Fe contents of the C-S-H phases (molar Fe(III)/Si $\leq$ 0.001; molar Fe(II)/Si $< 1 \times 10^{-9}$) based on the K_d values reported earlier by Mancini and co-workers [45,46].

For the non-exposed region of the *Seawater* sample (Fig. 6b/d/f), the predicted initial composition of the hydrate assemblage consisted of C-S-H, monocarbonate, hydrotalcite, and ettringite at a pH of 13.9. With increasing exposure to sea water, at first Kuzel's salt ($Ca_4Al_2(OH)_{12}Cl(SO_4)_{0.5}{\cdot}6H_2O$) and thereafter Friedel's salt formed. Eventually monocarbonate destabilizes and pH decreases further. The formation of ettringite, thaumasite, and gypsum was predicted to occur closer to the surface due to the presence of sulphate, carbonate, and magnesium in sea water. Friedel's salt, C-S-H phases and ettringite were predicted to decompose at the surface, leading to the formation of M-S-H phases,

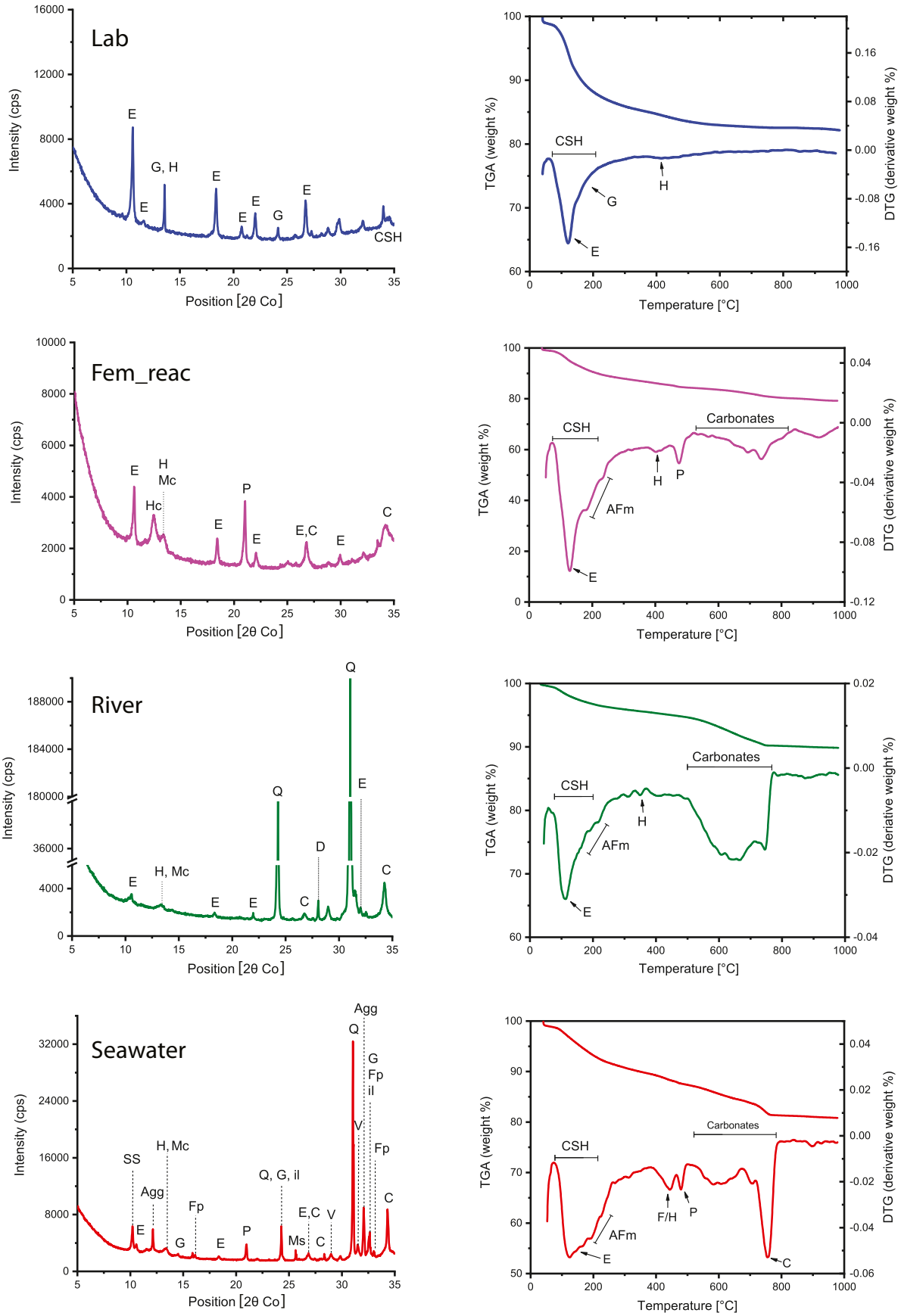

Fig. 4. X-ray diffraction profiles (left) and thermogravimetry analyses (DTG above and TGA below) for the investigated samples. Agg = undefined phase from aggregate, C = calcite, CSH = calcium-silicate-hydrate, D = dolomite, E = ettringite, F = Friedel's salt, Fp = feldspar, G = gypsum, Hc = hemicarbonate, H = hydrotalcite, il = ilmenite, Ms. = monosulphate, Mc = monocarbonate, P = portlandite, Q = quartz, SS = sheet silicates, and V = vaterite.

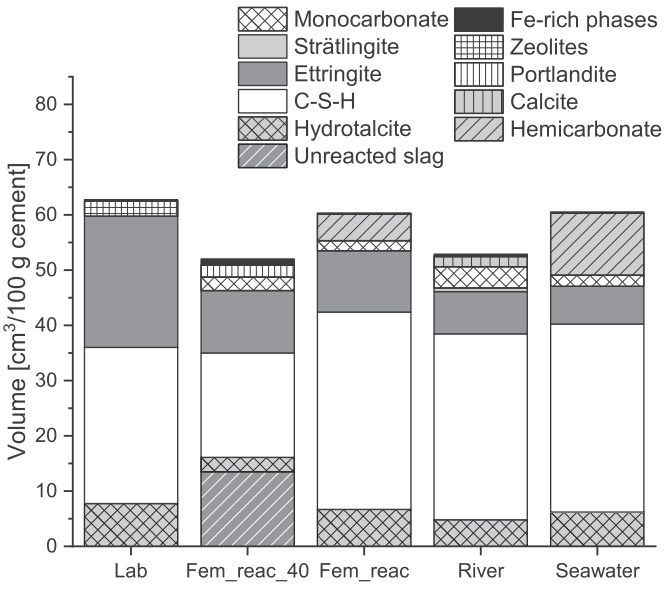

Fig. 5. Predicted volume of the hydrated cements assuming complete reaction for the *Lab*, *Fem_reac*, *River* and *Seawater* samples. A reaction degree of the slag of only 40% assumed in case of the *Fem_reac_40* sample. Note that in *Fem_reac_40* the Fe-rich phase is Fe-siliceous hydrogarnet.

carbonates, and hydrotalcite in agreement with the changes observed experimentally as reported elsewhere [10,74]. At the surface of concrete a pH of approximately 9 was calculated, controlled by the presence of calcite. In the hydrated, non-exposed blended cements troilite and magnetite were predicted as the Fe-containing phases. With increasing exposure to sea water, Fe-Si-hydrogarnet was predicted to be stable in a small range of sea water addition. At the highest exposure to sea water on the surface of the concrete, where oxidizing conditions dominate, Fe $(OH)_3$ was the only Fe-rich phase predicted with a small amount of Fe (III) taken up into the C-S-H phases in the stability range of C-S-H. Again, the amount of Fe(II) taken up by C-S-H phases was negligibly low. The evolution of the redox conditions in the *Seawater* sample was comparable to that in the *River* sample, i.e. negative E_h value at initial conditions and a strong increase after complete dissolution of magnetite and troilite.

3.2. Spectroscopic investigations of the bulk materials

In slag-containing cements, iron originates from two different sources. Fe(0) is present in the slag, while Portland cement contains Fe(III) in the clinker. In mortar and concrete samples (such as *Seawater* and *River*), Fe can also be present in the sand and aggregates. Fe K-edge XANES was employed to probe the chemical speciation of iron in the complex concrete matrices. The spectral contribution of the Fe-containing references was calculated for each XAS spectrum. The XANES spectra of representative Fe compounds (Fig. 2) show differences in the position of the absorption edge and the intensities of the spectral features across the white line. The different intensities of the latter features are caused by multiple scattering due to the neighbouring atoms. A shift in the absorption edge can either be attributed to the oxidation state or it can be caused by the different coordination geometry of Fe [64,65].

Fe references used for the identification of the Fe species had different iron oxidation states, such as Fe metal as iron 0; hibbingite (γ-$Fe_2(OH)_3Cl$) [23], FeS, FeS_2, $FeSO_4$, $FeCl_2$, ilmenite ($FeTiO_3$), and Fe $(OH)_2$ as iron +II; akaganeite (β-FeO(OH,Cl)) [23], FeOOH, Fe$(OH)_3$, Fe_2O_3, $Fe_2(SO_4)_3$, C_4AF, $FeCO_3$, $FeCl_3$, and Fe-siliceous hydrogarnet (Fe-Si-Hyd) as iron +III; Fe_3O_4 as iron +II and +III. Also Fe-doped C-S-H [45,46], AFm [42] and ettringite [76] were used in the fitting. Fe(0) represents the non-corroded iron in the slag and it was expected to be the main constituent in the samples in which little or no corrosion had occurred. C_4AF is the main clinker phase containing iron in the Portland cement. $FeCO_3$, FeO, Fe$(OH)_2$ Fe_3O_4, Fe_2O_3, FeOOH, and Fe$(OH)_3$ are main corrosion products of the reinforcement bars in concrete [39,40] and therefore, they were also expected to form when Fe(0) of the slag corrodes. Similarly, Fe-Si-Hyd, the most stable Fe(III)-containing cement phase in hydrated PC [31] could be present. Slag contains also reduced sulphur species and therefore mackinawite (FeS) and pyrrhotite ($Fe_{1-x}S$, $0 < x < 0.2$) [6] were expected to precipitate in slag-based cements [36]. Also green rust components, β-FeO(OH,Cl), and γ-$Fe_2(OH)_3Cl$ could be present as they are reported to form in the presence of Cl^- from sea water (for example [77–79]). In addition to these above-described Fe-rich compounds, ilmenite ($FeTiO_3$) could be present as it was found by XRD in the aggregates of the *Seawater* sample (see Section 3.3.3).

Principal component analysis (PCA) and iterative target-transformation (TT) analyses could not be used for *Lab* and *River* samples because the number of acquired spectra was below the limit required to provide realistic results (<6) and, as a consequence, the maximum number of component was set to 4. On the other hand, TT were successfully applied to calculate the SPOIL number and consequently to discard the unnecessary references for fitting the *Seawater* sample.

The bulk-XANES spectra recorded on the hydrated bulk samples (crushed material) were fitted between 7080 and 7200 eV in normalized μ(E) space by linear combination using the Fe references described above. Table 2 summarizes the contributions of the single Fe compounds to the XANES spectra of the *Lab*, *River and Seawater* bulk samples. The very low residual factor (R factor) suggests excellent agreement between modelled and experimental data (Fig. 7). The spectra of *Lab* and *River* shows similar spectroscopic features and Fe(0) was found to be the dominant compound in both samples (~79% and ~60%, respectively) along with approximately 10% of FeS. Other contributions to the spectrum of the *Lab* sample were ~11% Fe_3O_4, while the *River* sample contained in addition ~16% Fe-Si-Hyd, and ~14% goethite. The *Seawater* sample was the only slag-containing sample in which no Fe(0) was detected. Instead, ~44% Fe-Si-Hyd, ~20% Fe$(OH)_2$, ~19% FeO, and ~17% ilmenite were estimated to contribute to the XANES spectrum of the bulk *Seawater* sample. Ilmenite was found to be associated with the aggregates (Section 3.3.3).

The *Fem* samples allowed us to explore the evolution of the Fe components over time with and without sea water interaction (Table 3 and Fig. S1). Deconvolution of the bulk-XANES spectra of the *Fem* blended cement samples was applied to determine the contributions of the single Fe compounds to the unhydrated cement, a paste sample hydrated for 28 days, and the concrete samples exposed to sea water for 2 and 5 years. The Fe of the non-hydrated cement mainly consisted of two different Fe species, i.e. the Fe-rich clinker phase C_4AF (~54%) and Fe(0) (46%) from the slag. Nevertheless, the higher residual (R factor) indicates that there is an important Fe species in the slag cement which was not considered in the LC fitting, such as Fe in the glassy fraction of the slag. After 28 days of hydration, the C_4AF had reacted resulting in the release of Fe(III) and uptake into Fe-Si-Hyd (~33%). This is in agreement with observations made on aged PC, where Fe-Si-Hyd was found to be the dominant Fe-containing hydrate [42]. No significant reaction of Fe(0) was observed. The residual of the LC fitting improved as compared to the *Fem_unhyd* sample, suggesting that a portion of the unknown Fe fraction had reacted. Note that the proportions of Fe(0) in the *Fem_unhyd* and *Fem_react* samples should be the same, as Fe(0) has not reacted. The apparent increase is considered to be an artefact of the LC fitting due to the presence of the unknown Fe fraction.

The two samples exposed to sea water for 730 and 1825 days showed the presence of Fe-Si-Hyd (27% and 21% respectively), and instead of Fe (0), the presence of FeO (26% and 28%) and Fe_2O_3 (47% and 51%). The amount of Fe-Si-Hyd seems to decrease with increasing exposure to sea water, while the proportions determined by LC fitting could be in the range of the uncertainty of the method. Note that, in contrast to the *Lab*

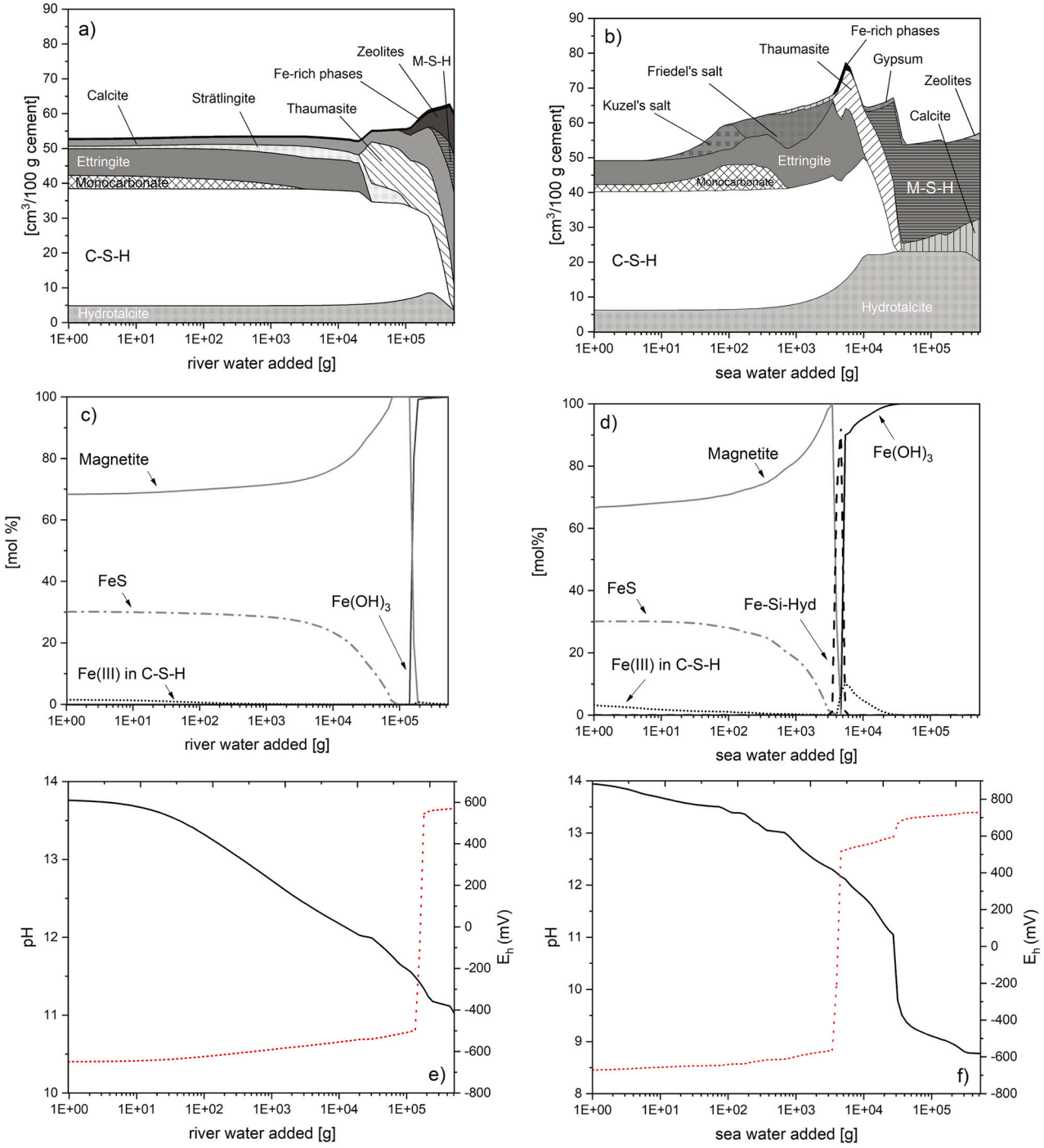

Fig. 6. Predicted volume of the phases in the two slag-containing cements *River* and *Seawater* upon exposure to increasing amounts of water based on thermodynamic modelling. a) Hydrate assemblage, c) Fe phases, and e) pH (solid line) and E_h (dotted line) of the *River* slag sample in contact with river water and, b) hydrate assemblage, d) Fe phases, and f) pH (solid line) and E_h (dotted line) of the *Seawater* slag sample in contact with North Sea sea water.

and *River* samples, Fe(0) was absent, respectively below the detection limit in the *Seawater* sample.

3.3. Micro-scale investigations

3.3.1. Redox maps

Fig. 8 shows the 2D distribution of the iron oxidation states in the *Lab*, *River and Seawater* samples. For each sample, several regions of interest (ROI) had been scanned which resulted in the same overall picture. Small particles of Fe(0) dominated the redox map in case of the *Lab* and the *River* samples, while the content of the Fe(II, III)-rich species was very low (Fig. 8a-d). The latter species were mostly detected at the boundary of Fe(0) particles.

In contrast, only few Fe(0) spots were detected in the *Seawater* sample (Fig. 8e/f). Fe was present mainly as Fe(II) with some Fe(III). This finding agrees well with the previous observations made on the sea water-treated *Fem* samples.

3.3.2. Lab and River samples

SEM image analysis corroborated that the *Lab* and *River* samples contained Fe(0)-containing slag particles. The particles had different shapes with regular and irregular boundaries and their size typically

Table 2
Proportions (%) of the Fe-containing phases in the XANES spectra of the *Lab*, *River* and *Seawater* samples as determined by LC fitting.

	Fe(0)	FeO	FeS	Fe_3O_4	$Fe(OH)_2$	Fe-Si-Hyd	FeOOH	$FeTiO_3$	R factor
	%	%	%	%	%	%	%	%	
Lab	79(10)	–	10(3)	11(3)	–	–	–	–	0.0002
River	60(7)	–	10(2)	–	–	16(2)	14(4)	–	0.0004
Seawater	–	19(3)	–	–	20(3)	44(6)	–	17(3)	0.0006

Number in brackets indicates error from the fit to the experimental data plus the estimated systematic error, 10% of the indicated absolute values, due to the possible presence of minor Fe-containing phases not considered in the fit. –: absent (or below 10%).
Reaction times: *Lab* = 6 years, *River* = 7 years, *Seawater* = 34 years.

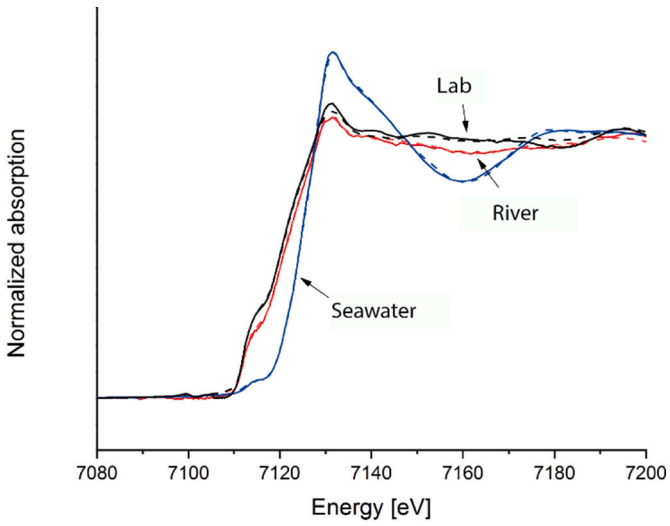

Fig. 7. Bulk XANES spectra for the three studied samples (full lines: experimental data, dashed lines: modelled data using LC).

Table 3
Proportions (%) of the Fe-containing phases in the XANES spectra of *Fem* samples as determined by LC fitting.

Sample	Age	C_4AF	Fe(0)	FeO	Fe_2O_3	Fe-Si-Hyd	R factor
Fem	days	%	%	%	%	%	
Fem_unhyd	–	54(6)	46(7)	–	–	–	0.0097
Fem_reac[a]	28	–	67(8)	–	–	33(4)	0.0061
Fem_2y[b]	730	–	–	26(5)	47(7)	27(5)	0.0013
Fem_5y[b]	1825	–	–	28(4)	51(7)	21(4)	0.0012

Number in brackets indicates error from the fit to the experimental data plus the estimated systematic error, 10% of the indicated absolute values, due to the possible presence of minor Fe-containing phases not considered in the fit; –: absent (or below 10%).
[a] Paste sample hydrated in the laboratory.
[b] Concrete samples exposed to sea water.

varied between 10 and 100 μm. The particles contained minor proportions of Ca, Si, P, and S in addition to Fe (Fig. 9 and Table 4).

Deconvolution of the XANES spectra collected at various ROIs again allowed us to discern the Fe speciation in the hydrated *Lab* and *River* samples at a micro-scale resolution (Table 5). In general, the Fe species determined from the micro data confirmed the trends already elaborated from the bulk data and the redox maps. For example, the micro data from the *Lab* sample showed a predominance of Fe(0) with minor contents of Fe_3O_4 and FeS, in line with the bulk results (Table 2). Only in one spot Fe_3O_4 was identified as the major component. The micro data also corroborated predominance of Fe(0) in the *River* sample. Note that in the *River* sample less Fe(0) particles were observed than in the *Lab* sample. In some ROIs, only FeS, FeOOH, $Fe(OH)_2$, and Fe-Si-Hyd were identified, while no Fe(0) was present. All the Fe compounds were previously identified in the bulk material except $Fe(OH)_2$, which could be a minor, locally prevailing compound, while its content is negligibly small on the bulk level.

3.3.3. *Seawater sample*

A significantly larger variety in the Fe speciation was noted in the *Seawater* sample, while Fe(0) particles were almost entirely absent. Around 40 micro-XANES spectra were collected in order to account for the inherent heterogeneity of the material. Nevertheless, PCA analysis did not provide a realistic number of minimal components, probably due to the high level of noise of the spectroscopic data [80]. Therefore, the number of components was arbitrary set to 5 and TT analysis was subsequently performed. The latter transformation revealed that $Fe(OH)_2$, FeO, Fe_2O_3, γ-$Fe_2(OH)_3Cl$, Fe_3O_4, FeOOH, $Fe(OH)_3$, β-FeO(OH,Cl), $FeTiO_3$, and Fe-Si-Hyd had SPOIL numbers <3 and thus, they were considered in the LC fitting (Table S3). FeO, Fe_2O_3, Fe_3O_4, $Fe(OH)_2$, and Fe-Si-hydrogarnet were the most common Fe-containing phases identified in the ROIs of the *Seawater* sample (Fig. S3) by LC fitting (Table 6).

Larger Fe(II)-containing particles (≥200 μm) were observed within the aggregates of the *Seawater* sample (Fig. 10). These particles had a high Ti content indicating the presence of ilmenite in agreement with the XRD observations (Fig. 11). The micro-XANES spectrum of Fe(II)-containing ilmenite was recorded on a Ti-rich aggregate particle (Fig. 10) and used as a reference in the LC fitting. Indeed, in some ROIs of the *Seawater* sample, the presence of ilmenite was clearly confirmed (data not shown), indicating that they were collected in the aggregates rather than in the slag.

The ilmenite aggregates in the *Seawater* sample were further characterized by micro-XRD combined with SEM measurements (Fig. 11). The XRF map of a typical aggregate revealed scattered globular regions rich in Ca, and a continuous region which also contained Ca but at a relatively low concentration (Fig. 11a). The same continuous region also contained Fe, within which hotspots of Fe were also observed (Fig. 11b). Highly Ti-concentrated regions were often found nearby the Fe-rich hotspots (Fig. 11c). Regions with elemental contrast were consistent with the greyscale heterogeneity in the SEM-BSE image (Fig. 11d). In a dark-to-bright order, five types of regions were defined (r1-r5). Region r1 and r2 corresponded to SiO_2 with negligible concentrations of Ca, Fe and Ti. Region r3 was the continuous area with intermediate concentrations of both Ca and Fe. Region r4 had similar greyscale as r3, yet it clearly corresponded to the globular region highly rich in Ca but poor in Fe. The brightest region (r5) corresponded to intermixed Fe-rich and Ti hotspots.

Results of the SEM-EDX analysis of these sub regions are summarized in Table 7. The region r1 was composed of only Si and O, i.e. SiO_2. The region r2 had a general composition of $(Na/K)Ca_{0.01}Al_{1.1}Si_{3.18}O_{9.6}$, and the measured spots were either overwhelmingly rich in Na or K. This chemical composition was generally consistent with feldspar with minor SiO_2 inclusions. The composition of region r3 was $(Na/K)_{0.2}Mg_{0.47}Ca_{0.53}Fe_{0.99}Ti_{0.04}Al_{0.4}Si_{2.08}O_{8.1}$, which may fit the pyroxene group. Region r4 had a composition of $CaF_{0.2}P_{0.58}Si_{0.02}O_{2.7}$, which fits the composition of fluoroapatite ($Ca_5(PO_4)_3F$) [81]. The region r5 was a mixture of a Ti-rich phase ($TiFe_{1.01}Mn_{0.08}Si_{0.01}O_{3.2}$) and a Ti-poor phase ($FeO_{1.4}$).

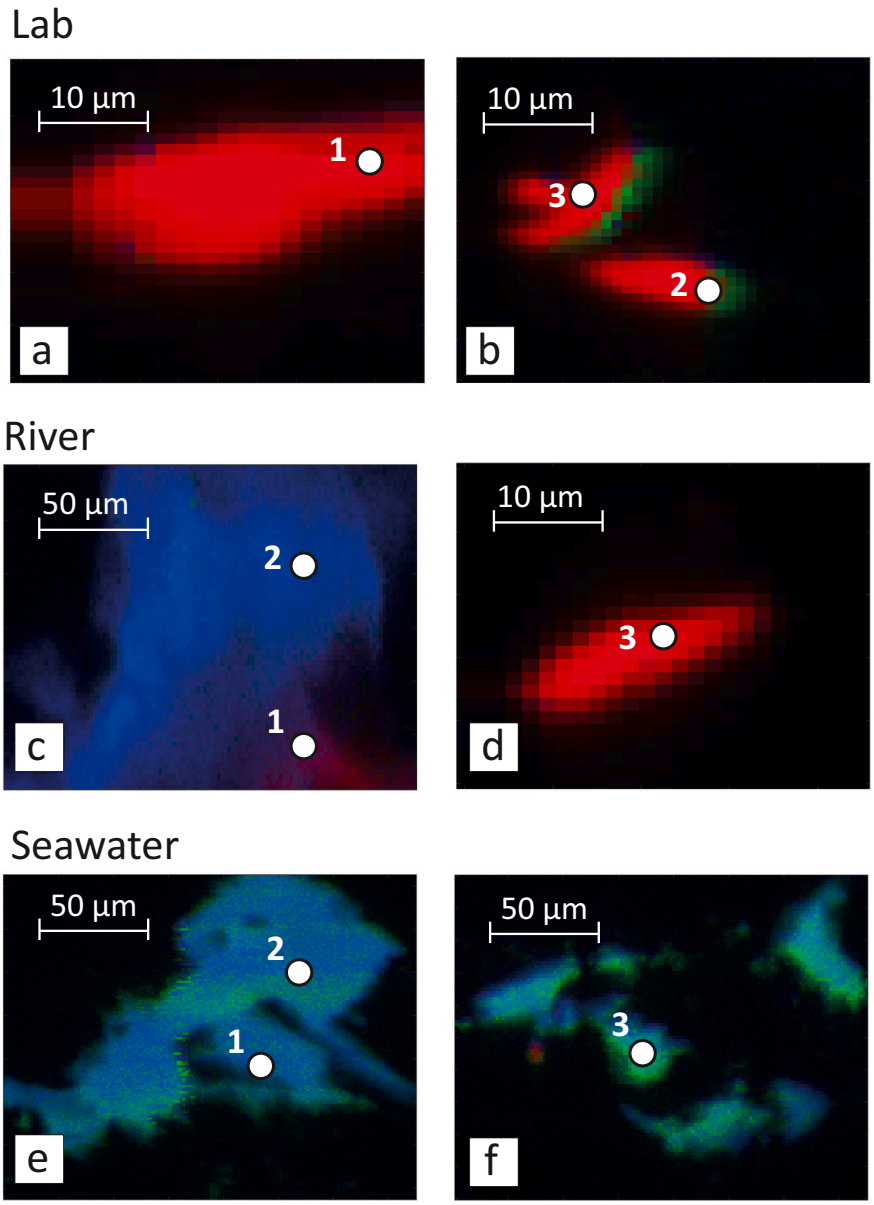

Fig. 8. Iron chemical distribution maps of two different regions of interest on the *Lab* (a, b), *River* (c, d) and *Seawater* (e, f) samples. Oxidation states are depicted in RGB colours with red = Fe(0), green = Fe(II), and blue = Fe(III). Numbers refer to the location of the micro-XANES ROIs fitted in Tables 5 and 6. (For interpretation of the references to colour in this figure legend, the reader is referred to the web version of this article.)

Further micro-mineralogical information of the micro regions were provided by the micro-XRD data. Based on the grey scale contrast in Fig. 11d, the diffractogram of each sub-region was determined by adding-up the XRD of several pixels at the centre of each sub-region. The diffractograms of the whole area was obtained by the summation of the XRD of all pixels on the detected area. They are together plotted in equivalent 2theta angle of Co *Kα* (Fig. 12a). As indicated by the peak positions of a few known structures (coloured bars in Fig. 12a), region r1 matches quartz, region r2 albite (Na-feldspar), and region r4 fluoroapatite. These assignments are also consistent with elemental compositions (Table 6). Diffraction peaks of region r5 indicated the co-existence of magnetite (Fe_3O_4) and ilmenite ($FeTiO_3$) [82], which also matched the two different sets of compositions of r5 (Table 7). Diffraction peaks of region r3 (asterisks in Fig. 12a) could not readily be assigned to any known structure, yet the peak positions (43.3°, 45.9°, 51.2°, 63.3° and 88.4°) seemed to partly match the crystals in the pyroxene group, e.g. augite ($(Ca,Na)(Mg,Fe,Al,Ti)(Si,Al)_2O_6$) and pigeonite ($(Mg,Fe,Ca)(Mg,Fe)Si_2O_6$) [83].

The diffraction data of each sub-region was then used to illustrate the phase distribution. For the XRD of each sub-region, the peak area of its 3–5 strongest diffraction peaks were calculated at each pixel, and used as the contrast for phase mapping. The individual XRD phase mapping was plotted in Fig. 12b (labelled with r1–r5). They were then merged to form an overall phase mapping, whose colour contrast feature is highly comparable to the greyscale feature of the SEM image (first two subplots in Fig. 12b). Note that the colour scale is proportional to XRD peak areas, which is quantitative within an individual phase, but not quantitative among different phases. The microscale investigation thus suggest the existence of Fe-bearing phases from the slag aggregate, i.e. magnetite, ilmenite and a Ca-Fe rich phase which may possess a pyroxene structure. No clear sign of Fe-containing hydration products was observed in this particular region.

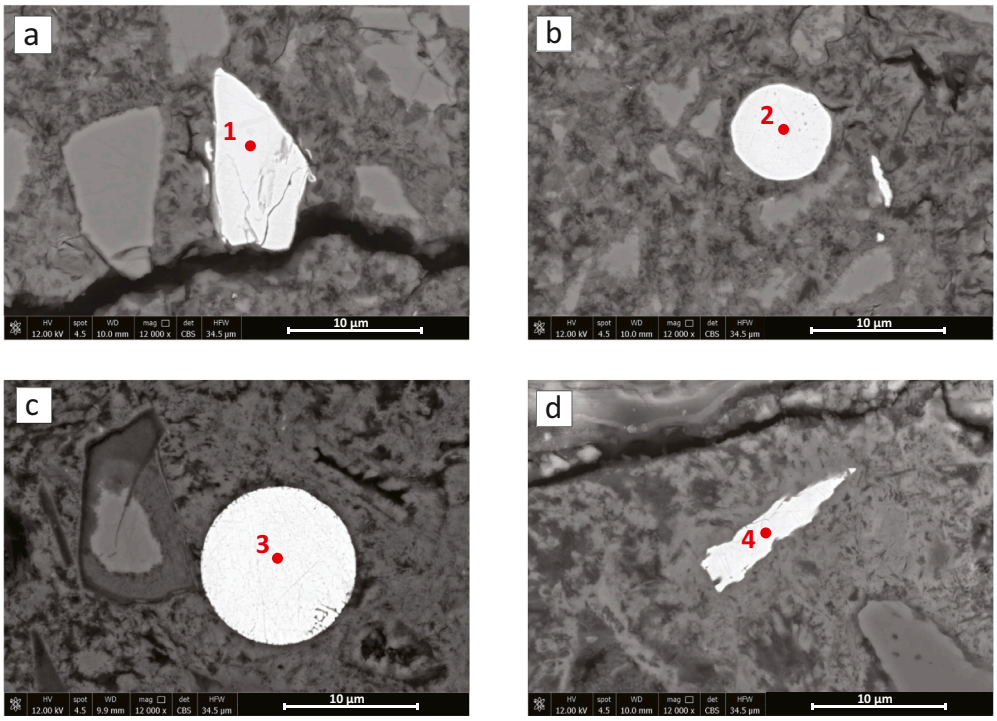

Fig. 9. SEM backscattered electron (BSE) of Fe particles of *Lab* (a, b) and *River* (c, d) samples. Points indicate location of quantitative analyses.

Table 4
Proportions (in atomic percentage) of the elements in the *Lab* and *River* samples determined from SEM-EDX point analysis.

Sample	Point	O	Fe	Si	P	S	Ca
		%	%	%	%	%	%
Lab	1	–	97.4	–	1.8	–	0.8
Lab	2	–	99.3	–	–	–	0.8
River	3	–	94.1	–	4.0	1.2	0.7
River	4	–	95.4	3.9	–	–	0.7

–: <0.1%.

4. Discussion

4.1. Composition of the hydrated cements

In this study iron speciation was investigated in a supersulfated slag cement (*lab*) and three blended slag Portland cements (*Fem*, *River* and *Seawater*). The development of thermodynamic models and the determination of the necessary thermodynamic data [59,84,85] enables to successfully predict the hydrate compositions in Portland cements under different environmental conditions [37,42,74,84,86,87]. Thermodynamic modelling as well as XRD and TGA data of the hydrated supersulphated slag cement (*lab*) indicated the presence of mainly C-S-H phases and ettringite plus some unreacted gypsum. The three blended slag cements (*Fem*, *River* and *Seawater*) predominantly contained C-S-H phases (and portlandite at early hydration times), and minor amounts of ettringite, AFm phases and hydrotalcite. The predicted results are generally in agreement with XRD and TGA measurements. In the supersulphated slag, the iron was predicted to be present mainly as FeS (troilite) and Fe_3O_4 (magnetite), while in the blended slag cements, where more CaO was available, in addition also siliceous hydrogarnet ($((CaO)_3(Al,Fe)_2O_3(SiO_2)_{0.84}(H_2O)_{4.32}$) was predicted and observed. Thermodynamic modelling also shows that the interaction with river and sea water can lead to a destabilisation of the C-S-H phases near the sample surface, to changes in the amount and kind of ettringite and AFm phases as well as to the oxidation of Fe(0) and Fe(II) to Fe(III).

The identification of Fe phases by XRD or TGA in the complex cement

Table 5
Proportions (%) of the Fe-containing phases in the micro-XANES spectra of the *Lab* and *River* samples as determined by LC fitting. The locations of the micro-XANES are shown in Fig. 8 (except for ROIs 4, which are shown in Fig. S3).

Sample	Fe(0)	FeS	F_3O_4	FeOOH	Fe-Si-Hyd	$Fe(OH)_2$	R factor
	%	%	%	%	%	%	
Lab_1	100(10)	–	–	–	–	–	0.0011
Lab_2	85(11)	–	15(4)	–	–	–	0.0012
Lab_3	90(10)	10(2)	–	–	–	–	0.0013
Lab_4	21(2)	–	79(9)	–	–	–	0.0006
River_1	58(9)	11(2)	–	31(6)	–	–	0.0004
River_2	–	–	–	39(6)	14(3)	47(9)	0.0005
River_3	100(10)	–	–	–	–	–	0.0012
River_4	–	–	–	47(7)	15(4)	37(8)	0.0015

Number in brackets indicates error from the fit to the experimental data plus the estimated systematic error, 10% of the indicated absolute values, due to the possible presence of minor Fe-containing phases not considered in the fit. –: absent (or below 10%).

Table 6
Proportions (%) of the Fe-containing phases in the micro-XANES spectra of the *Seawater* sample as determined by LC fitting.

Sample	FeO	F_2O_3	FeOOH	$Fe(OH)_2$	Fe_3O_4	Fe-Si-Hyd	γ-$Fe_2(OH)_3Cl$	β-FeO(OH,Cl)	R factor
	%	%	%	%	%	%	%	%	
Sea_1	33(5)	–	–	25(5)	26(4)	16(3)	–	–	0.0053
Sea_2	12(3)	10(2)	–	20(4)	–	–	58(8)	–	0.0038
Sea_3	–	18(4)	13(2)	–	–	52(7)	–	17(4)	0.0005
Sea_4	32(5)	16(3)	–	–	19(3)	33(5)	–	–	0.0032

Number in brackets indicates error from the fit to the experimental data plus the estimated systematic error, 10% of the indicated absolute values, due to the possible presence of minor Fe-containing phases not considered in the fit.

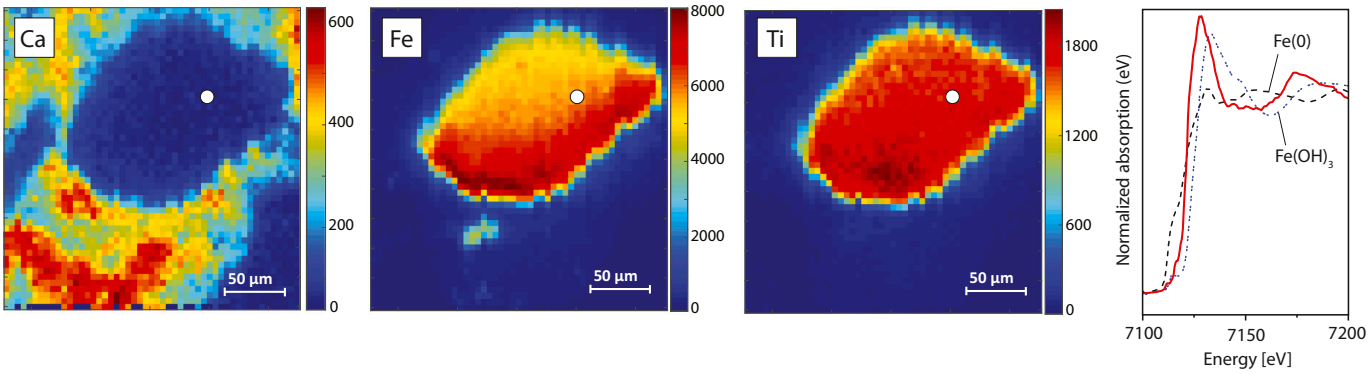

Fig. 10. XRF and XANES data of an ilmenite particle in the *Seawater* sample. Colour coded maps showing relative intensity from low (dark blue) to high (dark red). Comparison of the XANES data (red line) with those of Fe(0) (black dotted line) and $Fe(OH)_3$ (blue dotted line) indicates Fe(II). The XANES spectrum collected on this ROI was used as ilmenite reference spectrum. (For interpretation of the references to colour in this figure legend, the reader is referred to the web version of this article.)

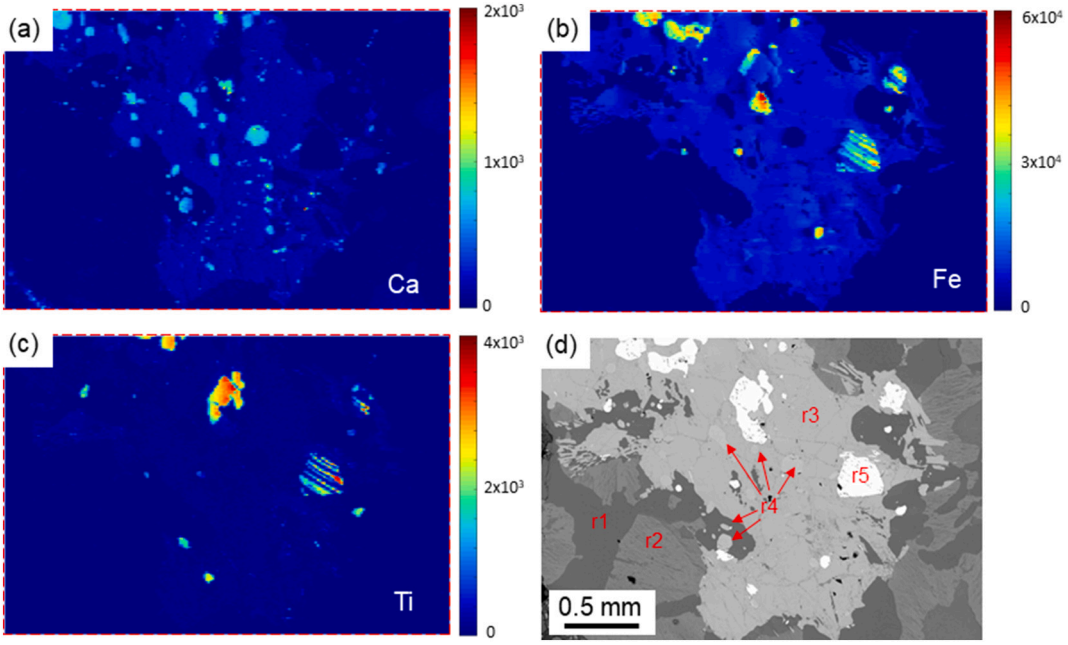

Fig. 11. Element mapping of the *seawater* sample: (a) Ca, (b) Fe and (c) Ti, and (d) SEM backscattered electron (BSE) image of the region of interest. Smaller regions of interest (r1-r5) were differentiated based on their greyscale contrast in the BSE image and elemental compositions.

matrix is difficult due to the overlapping of the Fe signals with other more common phases such as portlandite [42]. In addition, iron is present in cements as a minor component only making the detection even more challenging. In fact, except for ilmenite in the aggregate of the *Seawater* sample, no other Fe phases were detected by XRD or TGA. This is also illustrated in Fig. S2, where the Fe compounds used in the LC fitting of the spectroscopic data are indicated in the XRD pattern of the *Seawater* concrete. All the peaks of the iron phases overlap with those of major (hydrated) phases, making it impossible to unambiguously identify a minor quantity of those phases. Thus, the identification of Fe phases requires additional information such as thermodynamic modelling or element specific spectroscopic techniques.

Table 7
Averaged elemental compositions (in atomic percentage without oxides) of the sub region r1-r5. At least 10 ROIs were measured and averaged for each sub region, with an uncertainty of usually 5% of the corresponding value.

	O[a]	Na	Mg	Al	Si	K	Ca	Ti	Fe	F	P	Mn
	%	%	%	%	%	%	%	%	%	%	%	%
r1	*70*	–	–	–	30.3	–	–	–	–	–	–	–
r2_Na rich	*65*	6.9	–	7.4	21.0	–	0.2	–	–	–	–	–
r2_K rich	*65*	0.3	–	7.4	21.6	6.2	–	–	–	–	–	–
r3	*63*	1.2	3.7	3.1	16.2	0.4	4.2	0.3	7.7	–	–	–
r4	*60*	–	–	–	0.4	–	22.1	–	–	4.5	12.8	–
r5_Ti rich	*61*	–	–	–	0.1	–	–	18.9	19.0	–	–	1.5
r5_Ti poor	*58*	–	–	–	0.2	–	–	0.2	41.7	–	–	–

–: <0.1%.
[a] The determination of O by SEM/EDX is associated with a larger error (<10%) than those of elements with higher atomic numbers.

4.2. Iron sources in slag-containing concretes

Iron in slag-containing mortars and concretes can originate from the clinker, the slag, and the aggregates. In unhydrated Portland cement C_4AF is the only Fe source detected by XANES [42]. In a blended slag cement both the presence of Fe(III) from C_4AF in the PC clinker and Fe (0) from the slag was identified by XANES for the unhydrated *Fem* cement (Table 4). After 28 days of hydration, the reaction of C_4AF has led to the formation of siliceous hydrogarnet in the blended cement paste (*Fem_reac*), as previously observed for plain Portland cements [42]. The relatively high residual (R factor) for the unhydrated and 28 days hydrated samples could be due to the presence of Fe in the other clinker phases [88] as well as in the Si-glass of the slag component [3]. The detection of the latter species by XANES is difficult due to the poorly defined coordination geometry of Fe in glasses [89]. In fact, the R factor was lower after 28 days, when most of the clinker had reacted. It further decreased in the long-term sample, where also a major part of the slag is expected to have reacted [7].

The analysis of the *Seawater* concrete also revealed the presence of ilmenite particles in the rock aggregates, which contributed to the total Fe signal observed. Ilmenite was detected by bulk XRD measurements, SEM-EDX, micro-XRD, and bulk XAS analysis. A SEM-BSE image reveals an ilmenite particle embedded in an aggregate, which is intercalated with magnetite (Fig. 13). Note that the grain boundary of this particle does not show any reaction rim or other signs of dissolution, indicating that no significant reaction has occurred. This was also observed for other ilmenite particles.

4.3. Fe(0) oxidation in different environments

In all cases, some of the iron in the slag cements was initially present as Fe(0). No significant Fe(0) oxidation was observed in the *Fem* paste hydrated in the laboratory up to 28 days (Table 3). In the *Lab* sample (where only slag but no Portland cement was present), still 79% of Fe(0) was present after a reaction time of 6 years, indicating that at maximum 21% of the iron had oxidised (Table 2). The SEM-BSE (Fig. 9) and the redox mapping (Fig. 8) confirmed that only little oxidation has occurred.

Similar observations have been made for the concrete sample *River*, which still contains 60% of Fe(0) (Table 2). The morphology of the Fe(0) particles of the *River* sample are very similar to the ones detected in the *Lab* sample (Figs. 8 and 9). In addition, some Fe(III)-rich areas were observed (see for example Fig. 8c) in the redox maps, which are probably related to Fe-siliceous hydrogarnet formed from the ferrite in the clinker. Furthermore approximately 10% of FeS and 14% of $Fe(OH)_3$ have been observed, indicating some oxidation of Fe(0) during the 7 years of hydration. Also the exposure to the river water can be expected to have contributed to the observed partial iron oxidation as indicated by thermodynamic modelling (Fig. 6c), suggesting a slightly higher degree of oxidation in this sample than in the *Lab* sample.

The decisive effect of sea water on Fe(0) is visible in the *Fem* samples (Table 4). The sample *Fem_reac*, which was hydrated in the laboratory for 28 days, shows no significant Fe(0) oxidation in comparison with the unhydrated sample. After 2 and 5 years of exposure to sea water, however, Fe(0) is absent and FeO and Fe_2O_3 are present instead, thus indicating almost complete oxidation of the originally present Fe(0). In fact, in the *Seawater* sample, Fe(0) was detected only in a very small spot (<10 μm) in one of the regions investigated by redox mapping (Fig. 8f). Otherwise no Fe(0) was observed neither by SEM nor by micro-XRD indicating that very little Fe(0) remained in the *Seawater* sample hydrated and exposed to sea water for 34 years. In addition, the best fit of the bulk XANES spectrum did not indicate the presence of Fe(0), but it supported the presence of Fe(II), in FeO, $Fe(OH)_2$ and ilmenite and of Fe (III) in Fe-siliceous hydrogarnet (Table 2). All the micro-XANES data collected for the *Seawater* sample can be classified in an absolute energy Fe valence scatter plot originally developed by Marcus et al. [90] and updated since that time with a new custom Matlab code and additional Fe standards. This Fe valence plot is based on normalized absorption features at 7113 eV (i.e. μ) and 7115 eV (i.e. κ) as compared to known redox state standard compounds [90] and confirms the absence of Fe(0) in the *Seawater* sample (Fig. 14).

In summary, little oxidation of Fe(0) was observed in the absence of chloride, even in hydrated samples exposed to river water for 7 years. This indicates a strong passivation of Fe(0) under the latter conditions. In contrast, the presence of sea water, or more specifically of the chloride in the sea water, accelerates the corrosion of Fe(0) in the slag-containing cements significantly, such as in the *Fem_2y* samples after 2 years of exposure to sea water where the originally present Fe(0) was completely oxidised. Our observations of Fe(0) particles present in the slag agree well with previous reports on steel bars embedded in concrete. Steel bars remain protected from oxidation by a passive layer formed on the steel surface due to the high alkalinity of the cement pore solution [30]. Such passive films do not stop corrosion completely but strongly reduce the corrosion rate. The corrosion rate, however, will significantly increase if the passive layer is destroyed due to a reduction in alkalinity or if the chloride concentration increases (see references in [91,92]).

Corrosion under oxic conditions can be described by the following equation: $Fe(0) + 0.75\ O_2 + 0.5\ H_2O = FeOOH$. However, iron can also oxidise in the absence of oxygen via the reduction of H_2O: $3Fe(0) + 4\ H_2O = Fe_3O_4 + 4\ H_2$, resulting in the formation of magnetite and H_2. In the slag-containing cements reducing conditions are present [7]. The thermodynamic calculations indicate strongly reducing conditions in the *River* and *Seawater* samples with a redox potential of about −600 mV predicted for these slag-containing cements (Fig. 6e/f). The observed formation of FeS and magnetite in the *Lab* and *River* samples indicates the occurrence of anoxic iron corrosion, comparable to observations for steel embedded in concrete at anoxic conditions (for example [27,28]). In addition, in most samples also oxic oxidation seems to occur.

4.4. Corrosion products formed

The type of corrosion products formed is strongly influenced by

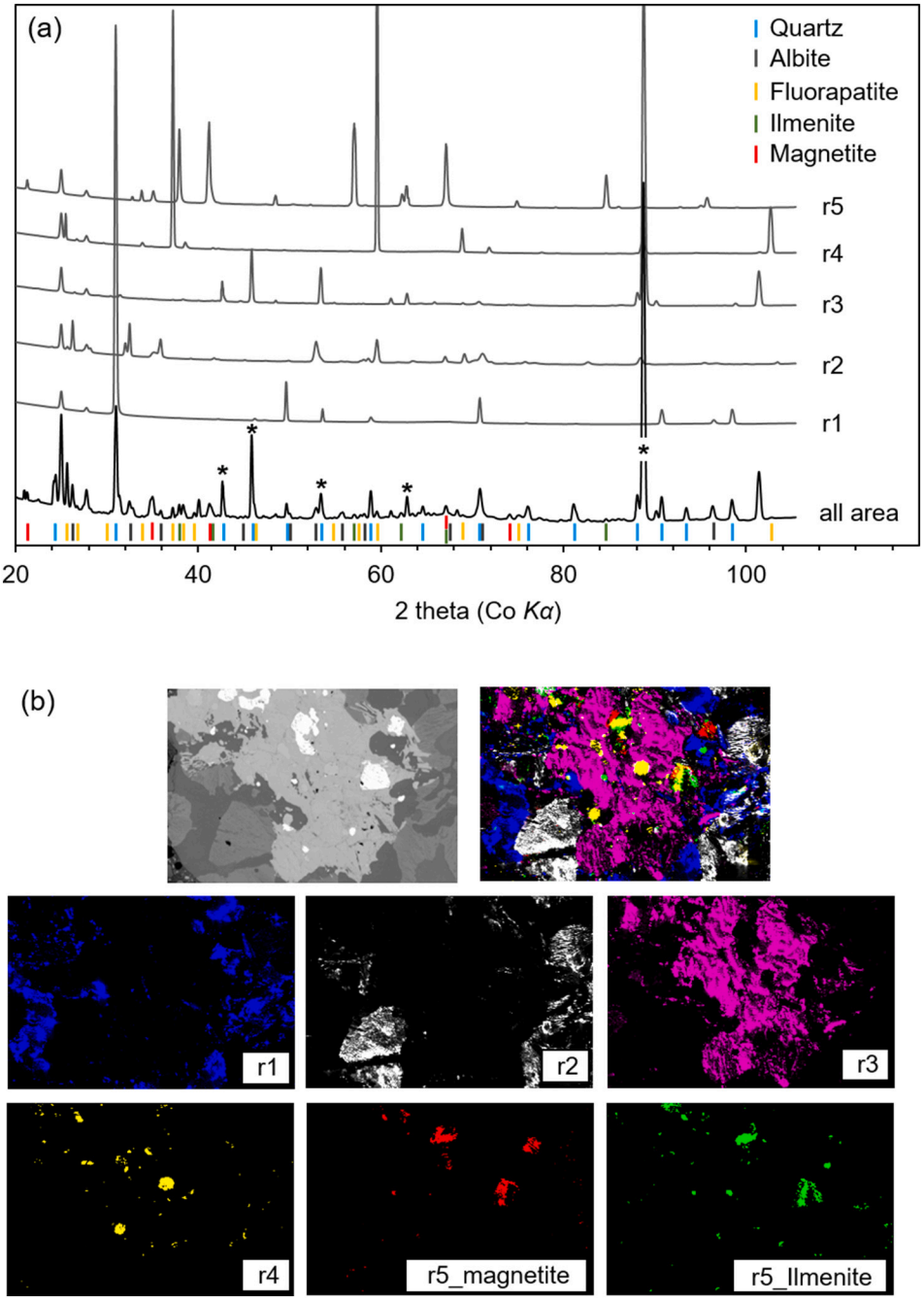

Fig. 12. Micro-XRD result of the areas of interest outlined in Fig. 11. (a) The diffractograms of the entire area and the sub regions. Peaks of assigned phases are labelled with vertical bars; peaks of region r3 are labelled with asterisks. b) Merged and individual mapping of each phase, in comparison with the SEM image.

environmental conditions and material properties [40]. LC fitting of bulk- and micro-XANES spectra indicate that, besides Fe(0) in the *River* and *Lab* samples, other Fe compounds are present. FeS, FeO, $Fe(OH)_2$, Fe_3O_4, FeOOH, Fe_2O_3, and Fe-siliceous hydrogarnet were the Fe-species identified in the aged samples and their formation very likely occurred upon oxidation of the initial Fe(0). Note that FeOOH, Fe_2O_3, and Fe-siliceous hydrogarnet can also form from the reaction of the iron(III) present in the clinker [42]. FeO, $Fe(OH)_2$, Fe_2O_3, Fe_3O_4 and FeOOH have been reported as corrosion products of steel embedded in concretes [39,40,93] and these Fe compounds have also been observed in archaeological artefacts [9,16,18,20,35,94,95]. Siliceous hydrogarnet, the main Fe-containing phase in hydrated Portland cement paste [31,32], has only very recently been identified for the first time as an oxidation product of steel in cements [28] in agreement with our observations presented here. The formation of FeS has been predicted by thermodynamic modelling in alkali activated, supersulphated and blended slag cements [6,37,96] as sulphur is present in the S(-II) chemical form in slags [97,98], reflecting the strongly reducing conditions. The XANES spectra recorded in this study confirmed experimentally the formation of FeS in the *Lab* and the *River* samples.

In contact with sea water, however, where chloride, moisture, and oxygen are available, corrosion of the iron can be expected [91,99]. The formation of Friedel's salt ($Ca_4Al_2Cl_2(OH)_{12}{\cdot}4H_2O$) as detected in the bulk *Seawater* sample (Fig. 4) suggest the presence of Cl^- in the sample and possibly also the formation of Fe-Cl-containing hydrates as reported elsewhere [9,23,100]. The possible formation of the latter phases was assessed by LC fitting of the XANES data and thermodynamic modelling. The LC fitting did not indicate the presence of Fe-Cl-rich phases, such as

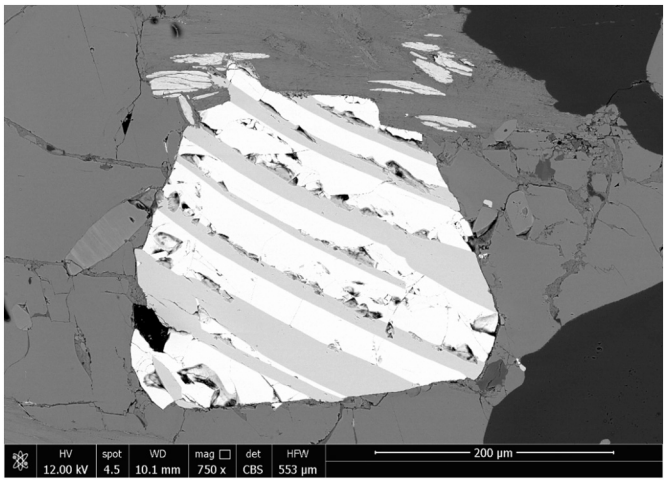

Fig. 13. Detail of an ilmenite particle in the slag. Ilmenite (grey stripes) is intercalated with magnetite (white stripes) as previously observed by Temple [82].

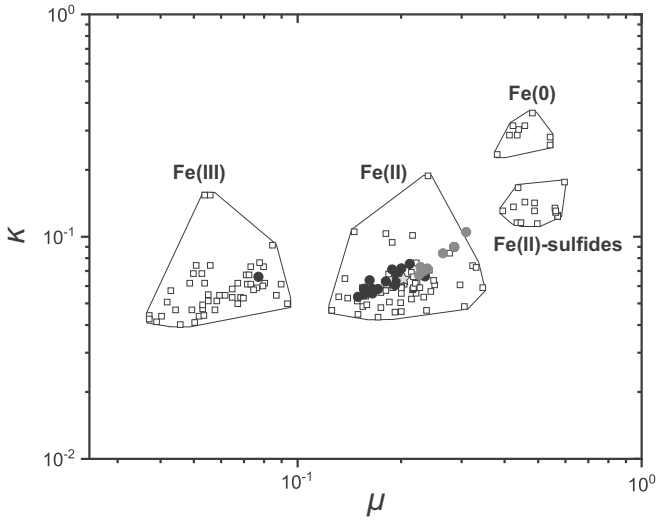

Fig. 14. Absolute energy Fe valence scatter plot generated from micro-XANES data collected on the *Seawater* sample. μ and κ represent the normalized XANES absorption values at 7113 eV and 7115 eV, respectively. Empty symbols represent the Fe-bearing standards of known oxidation state, while filled symbols indicate the *Seawater* sample (black: measured at ALS, grey: measured at SLS) and the filled star indicates the oxidation state of the ilmenite spectrum. Most of the data for the *Seawater* sample are in the Fe(II) region. Note that no measured data plotted in the Fe(0) region, indicating that no Fe(0) was present in the *Seawater* sample as confirmed by LC fitting. Note further that the data plotting in the Fe(II) region could be either pure Fe(II) or a combination of Fe (III) and Fe sulphides, see results of LCF fittings for more details.

akaganeite (β-FeO(OH,Cl)) and hibbingite (γ-$Fe_2(OH)_3Cl$) in the bulk material of the *Seawater* and *Fem* samples (Tables 2 and 3), which had both been exposed to Cl-containing sea water. Nevertheless, Fe-Cl-rich phases were identified on the micro-scale in some ROIs of the *Seawater* sample (Table 6). It should be noted that the LC fitting approach has its limitations: if an unknown species in the sample is not available as reference, it cannot be detected, and further low quantities of a phase (<10%) cannot be detected reliably. In addition, the mineral group can be reliably identified by the LC fitting approach, but not necessarily the precise identity of the mineral unless based and confirmed by other observations [101]. In some cases, e.g. iron sulphides, the identification is more reliable through XANES as their spectral features are pretty unique. As a consequence of this, interpretation of the LC fitting results cannot be based solely on the residual factor (R) but other information, such as additional analyses, chemical system, and external environments, must be considered as well. Hence, additional LC fitting was carried out with those spectra of the *Fem* and *Seawater* samples for which no Fe-Cl-rich phases had been identified based on the best fit approach, i.e. by considering the lowest residual as the sole criteria (Tables 2, 3 and 6). The compositions obtained from the supplementary fits are listed in Table 8 and they consider that the formation of Fe-Cl-phases could be expected due to exposure to sea water and the fitting cannot be based solely on the residual criteria. Hence, potential formation of akaganeite (β-FeO(OH,Cl)) and hibbingite (γ-$Fe_2(OH)_3Cl$) in the *Fem_2y* and *Fem_5Y* samples as well as in the *Seawater* sample (bulk, ROIs *sea_1* and *sea_4*) is indicated, while the residual factors are only slightly poorer than those for the best fits (Tables 2, 3 and 6). From these data, we may infer that Fe-Cl-rich phases could also be present in the two samples (*Fem*, *Seawater*) that had been exposed to sea water. The possible formation of akaganeite (β-FeO(OH,Cl)) and hibbingite (γ-$Fe_2(OH)_3Cl$) in the *Seawater* sample was further checked by thermodynamic modelling. In all calculations akaganeite (β-FeO(OH,Cl)) and hibbingite (γ-$Fe_2(OH)_3Cl$) were strongly under saturated (saturation index $< 10^{-10}$) indicating that their formation under water-saturated conditions is very unlikely. Note, however, that these phases might form at higher chloride concentrations as e.g. present in the tidal or the splash zones.

Oxidation of Fe(0) has consequences on the volume expansion of concrete as the molar volume of all oxidation products is larger than that of Fe(0) (Fig. 1). Nevertheless, volume expansion is expected to be small in those materials where Fe(0) corrosion is slow, such as in the conditions of the *Lab* and *River* samples. By contrast, larger volume changes are expected in cementitious materials exposed to sea water where the entire Fe(0) inventory has been converted into oxidised products.

5. Conclusion

A combination of synchrotron radiation-based methods, laboratory techniques, and thermodynamic modelling was used for investigating the speciation of iron in different slag-containing cements. Fe(III) present in the clinker (mainly in C_4AF), Fe(0) in the slag, and iron containing minerals ($FeTiO_3$) in the aggregates were identified as sources of iron in the concretes investigated in this study.

Table 8
Effect of Cl-rich phases on the LC fitting results of the *Seawater* (Sea) and *Femern* (Fem) samples.

Sample	FeO	Fe_2O_3	FeOOH	$Fe(OH)_2$	Fe_3O_4	Fe-Si-Hyd	γ-$Fe_2(OH)_3Cl$	β-FeO(OH,Cl)	$FeTiO_3$	R factor
	%	%	%	%	%	%	%	%	%	
Sea_bulk	–	–	–	–	–	47(7)	–	15(4)	26(6)	0.0007
Sea_1	32(4)	–	13(3)	–	–	–	55(9)	–	–	0.0077
Sea_4	41(6)	–	–	16(4)	15(4)	–	–	18(4)	–	0.0047
Fem_2y	–	18(4)	–	–	47(8)	16(4)	19(3)	–	–	0.0015
Fem_5y	–	31(5)	–	–	33(5)	18(4)	20(4)	–	–	0.0014

Number in brackets indicates error from the fit to the experimental data plus the estimated systematic error, 10% of the indicated absolute values, due to the possible presence of minor Fe-containing phases not considered in the fit. –: absent (or below 10%).

The phases observed generally agreed with predictions made, based on thermodynamic modelling, although some notable differences were observed. Thermodynamic modelling predicted the formation of FeS, Fe_3O_4, Fe-siliceous hydrogarnet and $Fe(OH)_3$ only, while experimentally Fe(0), FeO, $Fe(OH)_2$, FeS, Fe_3O_4, FeOOH, Fe_2O_3, and Fe-siliceous hydrogarnet were observed. This is probably due to kinetic effects and due to the high heterogeneity in the samples as observed by micro-XRF and micro-XANES.

Little oxidation of Fe(0) in hydrated slag cements was observed in the absence of chloride, even in samples exposed for 7 years to river water, indicating strong passivation of iron under these conditions. This agrees well with observations reported for steel bars embedded in concrete, which are passivated by the high pH of the cement pore solution. In addition, the formation of FeS and Fe_3O_4 was observed experimentally, indicating that reducing conditions in the samples were preserved and anoxic iron corrosion occurred.

In contrast, complete oxidation of Fe(0) was observed in the samples exposed to sea water, again in good agreement with strong acceleration of steel corrosion by chloride. Bulk- and micro-XANES studies indicate the formation of FeO, $Fe(OH)_2$, FeOOH, Fe_2O_3, and Fe-siliceous hydrogarnet by oxidation of the initial Fe(0). Whether or not Fe-Cl-rich phases, such as akaganeite and hibbingite, are also present in these samples could not be clearly assessed.

CRediT authorship contribution statement

A. Mancini: Methodology, Formal analysis, Investigation, Writing – Original Draft, Visualization.

B. Lothenbach: Conceptualization, Methodology, Formal analysis, Validation, Resources, Writing – Review & Editing, Supervision, Funding acquisition.

G. Geng: Formal analysis, Writing – Review & Editing.

D. Grolimund: Formal analysis, Investigation, Writing – Review & Editing.

D.F. Sanchez: Formal analysis, Investigation, Writing – Review & Editing.

S. Fakra: Formal analysis, Investigation, Writing – Review & Editing.

R. Dähn: Methodology, Data curation, Writing – Review & Editing, Supervision.

B. Wehrli: Writing – Review & Editing, Supervision.

E. Wieland: Conceptualization, Methodology, Validation, Data curation, Writing – Review & Editing, Supervision, Project administration, Funding acquisition.

Declaration of competing interest

The authors declare that they have no known competing financial interests or personal relationships that could have appeared to influence the work reported in this paper.

Acknowledgments

The authors wish to thank A. Ehrenberg (FEhS – Institut für Baustoff Forschung Duisburg, Germany) for providing the *River* sample from Auw an der Kyll, Germany and U.H. Jakobsen (DTI, Taastrup, Denmark) for providing the *Seawater* sample from the Vejle Fjord bridge and the set of *Fem* samples. Thanks are extended to F. Winnefeld (Empa) for the XRD measurements, A. Leemann (Empa) for the SEM analyses, D. Miron (PSI) for assistance with the thermodynamic modelling, and S. Réguer (SOLEIL) for providing the XANES spectra of akaganeite and hibbingite. D. Banerjee is thanked for assistance at BM26 (Dubble) and the ESRF for the provision of beamtime. G. Landrot is thanked for assistance at the Samba beamline and SOLEIL for the provision of beamtime. We acknowledge the Paul Scherrer Institut, Villigen, Switzerland, for provision of synchrotron radiation beamtime at the microXAS beamline of the Swiss Light Source (SLS). We acknowledge the Advanced Light Source at Lawrence Berkeley National Laboratory for provision of synchrotron radiation beamtime at XFM beamline 10.3.2. This research used resources of the Advanced Light Source, a DOE Office of Science User Facility under contract no. DE-AC02-05CH11231. Financial support by the Swiss National Science Foundation (grant no. 200021_162342) is kindly acknowledged. G. Geng wants to acknowledge the European Union's Horizon 2020 research and innovation program under the Marie Skłodowska-Curie grant agreement No 701647.

Appendix A. Supplementary data

Supplementary information section contains two tables and two figures. The river and sea water compositions used for calculating the water effect on the samples is shown in Table S1. Fig. S1 shows the XANES spectra of the bulk *Fem* samples. Fig. S2 shows the XRD diffractogram of the *Seawater* sample fitted by considering only the Fe-phases. Table S2 contains the PC and slag XRF analyses used for calculating the *Fem_reac_40* composition (34% PC and 66% slag), while Table S3 shows the results of target transformation. Fig. S3 shows the micro-XRF maps of Fe and the location of the analyses in the three investigated samples. Supplementary data to this article can be found online at https://doi.org/10.1016/j.cemconres.2020.106287.

References

[1] R.M. Andrew, Global CO_2 emissions from cement production, 1928–2018, Earth System Science Data, 11, 2019.
[2] K.L. Scrivener, V.M. John, E.M. Gartner, Eco-efficient cements: potential economically viable solutions for a low-CO_2 cement-based materials industry, Cem. Concr. Res. 114 (2018) 2–26.
[3] N.M. Piatak, M.B. Parsons, R.R. Seal II, Characteristics and environmental aspects of slag: a review, Appl. Geochem. 57 (2015) 236–266.
[4] U.S.G. Survey, Mineral Commodity Survey 2019, U.S. Geological Survey, 2019.
[5] S.A. Bernal, V. Rose, J.L. Provis, The fate of iron in blast furnace slag particles during alkali-activation, Mater. Chem. Phys. 146 (2014) 1–5.
[6] A. Gruskovnjak, B. Lothenbach, L. Holzer, R. Figi, F. Winnefeld, Hydration of alkali-activated slag: comparison with ordinary Portland cement, Adv. Cem. Res. 18 (2006) 119–128.
[7] B. Lothenbach, G. Le Saout, M. Ben Haha, R. Figi, E. Wieland, Hydration of a low-alkali CEM III/B-SiO_2 cement (LAC), Cem. Concr. Res. 42 (2012) 410–423.
[8] S. Mundra, M. Criado, S.A. Bernal, J.L. Provis, Chloride-induced corrosion of steel rebars in simulated pore solutions of alkali-activated concretes, Cem. Concr. Res. 100 (2017) 385–397.
[9] M. Bouchar, E. Foy, D. Neff, P. Dillmann, The complex corrosion system of a medieval iron rebar from the Bourges' Cathedral. Characterization and reactivity studies, Corros. Sci. 76 (2013) 361–372.
[10] U.H. Jakobsen, K. De Weerdt, M.R. Geiker, Elemental zonation in marine concrete, Cem. Concr. Res. 85 (2016) 12–27.
[11] L. Nilsson, E. Poulsen, P. Sandberg, H. Sørensen, O. Klinghoffer, HETEK, Chloride Penetration Into Concrete, State-of-the-art, Transport Processes, Corrosion Initiation, Test Methods and Prediction Models, Denmark, ISSN/ISBN, 1996, pp. 0909–4288.
[12] L. Bertolini, B. Elsener, P. Pedeferri, E. Redaelli, R.B. Polder, Corrosion of Steel in Concrete: Prevention, Diagnosis, Repair, John Wiley & Sons, 2013.
[13] P. Dillmann, D. Neff, D. Féron, Archaeological analogues and corrosion prediction: from past to future. A review, Corros. Eng. Sci. Tech., 49 (2014) 567–576.
[14] D. Neff, M. Saheb, J. Monnier, S. Perrin, M. Descostes, V. L'Hostis, D. Crusset, A. Millard, P. Dillmann, A review of the archaeological analogue approaches to predict the long-term corrosion behaviour of carbon steel overpack and reinforced concrete structures in the French disposal systems, J. Nucl. Mater. 402 (2010) 196–205.
[15] J. Monnier, L. Bellot-Gurlet, D. Baron, D. Neff, I. Guillot, P. Dillmann, A methodology for Raman structural quantification imaging and its application to iron indoor atmospheric corrosion products, J. Raman Spectrosc. 42 (2011) 773–781.
[16] D. Neff, P. Dillmann, L. Bellot-Gurlet, G. Beranger, Corrosion of iron archaeological artefacts in soil: characterisation of the corrosion system, Corros. Sci. 47 (2005) 515–535.
[17] W.J. Chitty, P. Dillmann, V. L'Hostis, C. Lombard, Long-term corrosion resistance of metallic reinforcements in concrete - a study of corrosion mechanisms based on archaeological artefacts, Corros. Sci. 47 (2005) 1555–1581.
[18] A. Michelin, E. Drouet, E. Foy, J. Dynes, D. Neff, P. Dillmann, Investigation at the nanometre scale on the corrosion mechanisms of archaeological ferrous artefacts by STXM, J. Anal. At. Spectrom. 28 (2013) 59–66.
[19] J. Monnier, D. Neff, S. Reguer, P. Dillmann, L. Bellot-Gurlet, E. Leroy, E. Foy, L. Legrand, I. Guillot, A corrosion study of the ferrous medieval reinforcement of

the Amiens cathedral. Phase characterisation and localisation by various microprobes techniques, Corros. Sci. 52 (2010) 695–710.
[20] P. Dillmann, D. Neff, F. Mazaudier, S. Hoerle, P. Chevallier, G. Beranger, Characterisation of iron archaeological analogues using micro diffraction under synchrotron radiation. Application to the study of long term corrosion behaviour of low alloy steels, J. Phys. 12 (2002) 393–408.
[21] J. Monnier, S. Reguer, D. Vantelon, P. Dillmann, D. Neff, I. Guillot, X-rays absorption study on medieval corrosion layers for the understanding of very long-term indoor atmospheric iron corrosion, Appl. Phys. A – Mat. 99 (2010) 399–406.
[22] M. Saheb, D. Neff, P. Dillmann, H. Matthiesen, E. Foy, Long-term corrosion behaviour of low-carbon steel in anoxic environment: characterisation of archaeological artefacts, J. Nucl. Mater. 379 (2008) 118–123.
[23] S. Réguer, F. Mirambet, C. Rémazeilles, D. Vantelon, F. Kergourlay, D. Neff, P. Dillmann, Iron corrosion in archaeological context: structural refinement of the ferrous hydroxychloride β-$Fe_2(OH)_3Cl$, Corros. Sci. 100 (2015) 589–598.
[24] T. Misawa, T. Kyuno, W. Suetaka, S. Shimodai, Mechanism of atmospherich rusting and effect of Cu and P on rust formation of low alloy steels, Corros. Sci. 11 (1971) 35–48.
[25] T. Misawa, Thermodynamic consideration for Fe-H_2O system at 25°C, Corros. Sci. 13 (1973) 659–676.
[26] G. Duffó, W. Morris, I. Raspini, C. Saragovi, A study of steel rebars embedded in concrete during 65 years, Corros. Sci. 46 (2004) 2143–2157.
[27] W. Lopez, J. Gonzalez, Influence of the degree of pore saturation on the resistivity of concrete and the corrosion rate of steel reinforcement, Cem. Concr. Res. 23 (1993) 368–376.
[28] D. Pally, P. Le Bescop, M.L. Schlegel, F. Miserque, L. Chomat, D. Neff, V. L'Hostis, Corrosion behavior of iron plates in cementitious solution at 80°C in anaerobic conditions, Corros. Sci. 170 (2020) 108650.
[29] R. O'Donovan, B.D. O'Rourke, K.D. Ruane, J.J. Murphy, Anaerobic corrosion of reinforcement, Key Eng. Mater. 569 (2013) 1124–1131.
[30] J.P. Broomfield, Corrosion of Steel in Concrete: Understanding, Investigation and Repair, CRC Press, 2003.
[31] M. Vespa, E. Wieland, R. Dähn, B. Lothenbach, Identification of the thermodynamically stable Fe-containing phase in aged cement pastes, J. Am. Ceram. Soc. 98 (2015) 2286–2294.
[32] B.Z. Dilnesa, B. Lothenbach, G. Renaudin, A. Wichser, D. Kulik, Synthesis and characterization of hydrogarnet $Ca_3(Al_xFe_{1-x})_2(SiO_4)_y(OH)_{4(3-y)}$, Cem. Concr. Res. 59 (2014) 96–111.
[33] M. Saheb, M. Descostes, D. Neff, H. Matthiesen, A. Michelin, P. Dillmann, Iron corrosion in an anoxic soil: comparison between thermodynamic modelling and ferrous archaeological artefacts characterised along with the local in situ geochemical conditions, Appl. Geochem. 25 (2010) 1937–1948.
[34] F. Mercier-Bion, J. Li, H. Lotz, L. Tortech, D. Neff, P. Dillmann, Electrical properties of iron corrosion layers formed in anoxic environments at the nanometer scale, Corros. Sci. 137 (2018) 98–110.
[35] Y. Leon, M. Saheb, E. Drouet, D. Neff, E. Foy, E. Leroy, J. Dynes, P. Dillmann, Interfacial layer on archaeological mild steel corroded in carbonated anoxic environments studied with coupled micro and nano probes, Corros. Sci. 88 (2014) 23–35.
[36] A. Gruskovnjak, B. Lothenbach, F. Winnefeld, R. Figi, S.C. Ko, M. Adler, U. Mäder, Hydration mechanisms of super sulphated slag cement, Cem. Concr. Res. 38 (2008) 983–992.
[37] B. Lothenbach, A. Gruskovnjak, Hydration of alkali-activated slag: thermodynamic modelling, Adv. Cem. Res. 19 (2007) 81–92.
[38] C.N. Singman, Atomic volume and allotropy of the elements, J. Chem. Educ. 61 (1984) 137.
[39] S.J. Jaffer, C.M. Hansson, Chloride-induced corrosion products of steel in cracked-concrete subjected to different loading conditions, Cem. Concr. Res. 39 (2009) 116–125.
[40] A. Köliö, M. Honkanen, J. Lahdensivu, M. Vippola, M. Pentti, Corrosion products of carbonation induced corrosion in existing reinforced concrete facades, Cem. Concr. Res. 78 (2015) 200–207.
[41] M.R. Lee, P.A. Bland, Mechanisms of weathering of meteorites recovered from hot and cold deserts and the formation of phyllosilicates, Geochim. Cosmochim. Acta 68 (2004) 893–916.
[42] B.Z. Dilnesa, E. Wieland, B. Lothenbach, R. Dähn, K.L. Scrivener, Fe-containing phases in hydrated cements, Cem. Concr. Res. 58 (2014) 45–55.
[43] B.Z. Dilnesa, B. Lothenbach, G. Le Saout, G. Renaudin, A. Mesbah, Y. Filinchuk, A. Wichser, E. Wieland, Iron in carbonate containing AFm phases, Cem. Concr. Res. 41 (2011) 311–323.
[44] B.Z. Dilnesa, B. Lothenbach, G. Renaudin, A. Wichser, E. Wieland, H. Jennings, Stability of monosulfate in the presence of iron, J. Am. Ceram. Soc. 95 (2012) 3305–3316.
[45] A. Mancini, E. Wieland, G. Geng, R. Dähn, B. Wehrli, B. Lothenbach, Fe(III) uptake by calcium silicate hydrates, Appl. Geochem. 113 (2020) 104460.
[46] A. Mancini, E. Wieland, G. Geng, B. Lothenbach, E. Wehrli, R. Dähn, Fe(II) interaction with cement phases: Method development, wet chemical studies and X-ray absorption spectroscopy, J. Coll. Interf. Sci., submitted.
[47] M. Vespa, R. Dähn, E. Gallucci, D. Grolimund, E. Wieland, A.M. Scheidegger, Microscale investigations of Ni uptake by cement using a combination of scanning electron microscopy and synchrotron-based techniques, Environ. Sci. Technol. 40 (2006) 7702–7709.
[48] M. Vespa, R. Dähn, D. Grolimund, E. Wieland, A.M. Scheidegger, Spectroscopic investigation of Ni speciation in hardened cement paste, Environ. Sci. Technol. 40 (2006) 2275–2282.
[49] E. Wieland, N. Macé, R. Dähn, D. Kunz, J. Tits, Macro-and micro-scale studies on U(VI) immobilization in hardened cement paste, J. Radioanal. Nucl. Chem. 286 (2010) 793–800.
[50] E. Wieland, R. Dähn, M. Vespa, B. Lothenbach, Micro-spectroscopic investigation of Al and S speciation in hardened cement paste, Cem. Concr. Res. 40 (2010) 885–891.
[51] E. Curti, D. Grolimund, C.N. Borca, A micro-XAS/XRF and thermodynamic study of CeIII/IV speciation after long-term aqueous alteration of simulated nuclear waste glass: relevance for predicting Pu behavior? Appl. Geochem. 27 (2012) 56–63.
[52] D. Grolimund, M. Senn, M. Trottmann, M. Janousch, I. Bonhoure, A. Scheidegger, M. Marcus, Shedding new light on historical metal samples using micro-focused synchrotron X-ray fluorescence and spectroscopy, Spectrochim. Acta B 59 (2004) 1627–1635.
[53] P. Clausen, At bygge bro, Dansk Betondag, 1991.
[54] Vejdirektoratet, Kystbroprojektet by Vejdirektoratet. Vejdirektoratet, 2000.
[55] M. Ben Haha, B. Lothenbach, G. Le Saout, F. Winnefeld, Influence of slag chemistry on the hydration of alkali-activated blast-furnace slag — part II: effect of Al_2O_3, Cem. Concr. Res. 42 (2012) 74–83.
[56] D.A. Kulik, T. Wagner, S.V. Dmytrieva, G. Kosakowski, F.F. Hingerl, K. V. Chudnenko, U.R. Berner, GEM-Selektor geochemical modeling package: revised algorithm and GEMS3K numerical kernel for coupled simulation codes, Comput. Geosci. 17 (2013) 1–24.
[57] W. Hummel, U. Berner, E. Curti, F. Pearson, T. Thoenen, Nagra/PSI chemical thermodynamic data base 01/01, Radiochim. Acta 90 (2002) 805–813.
[58] T. Thoenen, W. Hummel, U. Berner, E. Curti, The PSI/Nagra Chemical Thermodynamic Database 12/07, Paul Scherrer Institut, Villigen PSI, Switzerland, 2014.
[59] B. Lothenbach, D. Kulik, T. Matschei, M. Balonis, L.G. Baquerizo, B.Z. Dilnesa, G. D. Miron, D. Myers, Cemdata18: a thermodynamic database for hydrated Portland cements and alkali-activated materials, Cem. Concr. Res. 115 (2019) 472–506.
[60] R.J. Myers, S.A. Bernal, J.L. Provis, A thermodynamic model for C-(N-)ASH gel: CNASH_ss. Derivation and validation, Cem. Concr. Res. 66 (2014) 27–47.
[61] C. Rémazeilles, P. Refait, Formation, fast oxidation and thermodynamic data of Fe (II) hydroxychlorides, Corros. Sci. 50 (2008) 856–864.
[62] C.L. Snow, S.J. Smith, B.E. Lang, Q. Shi, J. Boerio-Goates, B.F. Woodfield, A. Navrotsky, Heat capacity studies of the iron oxyhydroxides akaganéite (β-FeOOH) and lepidocrocite (γ-FeOOH), The J. Chem. Thermod. 43 (2011) 190–199.
[63] J. Bourdoiseau, R. Sabot, M. Jeannin, F. Termemil, P. Refait, Determination of standard Gibbs free energy of formation of green rusts and its application to the Fe (II–III) hydroxy-oxalate, Colloids Surf. A Physicochem. Eng. Asp. 410 (2012) 72–80.
[64] B.K. Teo, Inorganic Chemistry Concepts, EXAFS: Basic Principles and Data Analysis, Springer-Verlag, Berlin/Heidelberg, 1986.
[65] D. Konigsberger, R. Prins, X-ray Absorption: Principles, Applications, Techniques of EXAFS, SEXAFS and XANES 159, Wiley/Interscience, New York, 1988, p. 160.
[66] B. Ravel, M. Newville, ATHENA, ARTEMIS, HEPHAESTUS: data analysis for X-ray absorption spectroscopy using IFEFFIT, J. Synchrotron Radiat. 12 (2005) 537–541.
[67] A.M. Scheidegger, D. Grolimund, M. Harfouche, M. Willimann, B. Meyer, R. Dähn, D. Gavillet, M. Nicolet, P. Heimgartner, The Micro-XAS Beamline at the Swiss Light Source (SLS): A New Analytical Facility Suited for X-ray Micro-beam Investigations With Radioactive Samples, Speciation Techniques and Facilities for Radioactive Materials at Synchrotron Light Sources, NEA Report, 2006, pp. 81–86.
[68] M.A. Marcus, A.A. MacDowell, R. Celestre, A. Manceau, T. Miller, H.A. Padmore, R.E. Sublett, Beamline 10.3. 2 at ALS: a hard X-ray microprobe for environmental and materials sciences. J. Synchrotron. Radiat., 11 (2004), 239–247.
[69] J.C. Fuggle, N. Mårtensson, Core-Level Binding Energies in Metals, J. Electron Spectrosc. Relat. Phenom. 21 (1980) 275.
[70] S. Kraft, J. Stümpel, P. Becker, U. Kuetgens, High resolution x-ray absorption spectroscopy with absolute energy calibration for the determination of absorption edge energies, Rev. Sci. Instrum. 67 (1996) 681–687.
[71] D.F. Sanchez, D. Grolimund, M. Hubert, P. Bleuet, J. Laurencin, A 2D and 3D X-ray μ-diffraction and μ-fluorescence study of a mixed ionic electronic conductor, Int. J. Hydrog. Energy 42 (2017) 1203–1211.
[72] E.R. Malinowski, Theory of error for target factor analysis with applications to mass spectrometry and nuclear magnetic resonance spectrometry, Anal. Chim. Acta 103 (1978) 339–354.
[73] S. Webb, SIXpack: a graphical user interface for XAS analysis using IFEFFIT, Phys. Scr. 2005 (2005) 1011–1014.
[74] K. De Weerdt, B. Lothenbach, M. Geiker, Comparing chloride ingress from seawater and NaCl solution in Portland cement mortar, Cem. Concr. Res. 115 (2019) 80–89.
[75] B. Lothenbach, B. Bary, P. Le Bescop, T. Schmidt, N. Leterrier, Sulfate ingress in Portland cements, Cem. Concr. Res. 40 (2010) 1211–1225.
[76] G. Möschner, B. Lothenbach, J. Rose, A. Ulrich, R. Figi, R. Kretzschmar, Solubility of Fe–ettringite ($Ca_6[Fe(OH)_6]_2(SO_4)_3{\cdot}26H_2O$), Geochim. Cosmochim. Acta 72 (2008) 1–18.
[77] C. Rémazeilles, D. Neff, F. Kergourlay, E. Foy, E. Conforto, E. Guilminot, S. Reguer, P. Refait, P. Dillmann, Mechanisms of long-term anaerobic corrosion of iron archaeological artefacts in seawater, Corros. Sci. 51 (2009) 2932–2941.

[78] H. Simon, G. Cibin, P. Robbins, S. Day, C. Tang, I. Freestone, E. Schofield, A synchrotron-based study of the Mary Rose iron cannonballs, Angew. Chem. Int. Ed. 57 (2018) 7390–7395.
[79] A. Gismelseed, M. Elzain, A. Yousif, A. Al Rawas, I. Al-Omari, H. Widatallah, A. Rais, Identification of Corrosion Products Due to Seawater and Fresh Water, ICAME 2003, Springer 2004, pp. 487–492.
[80] A. Manceau, M. Marcus, T. Lenoir, Estimating the number of pure chemical components in a mixture by X-ray absorption spectroscopy, J. Synchrotron Radiat. 21 (2014) 1140–1147.
[81] K. Sudarsanan, P. Mackie, R. Young, Comparison of synthetic and mineral fluorapatite, $Ca_5(PO_4)_3F$, in crystallographic detail, Mater. Res. Bull. 7 (1972) 1331–1337.
[82] A.K. Temple, Alteration of ilmenite, Econ. Geol. 61 (1966) 695–714.
[83] Y. Nakamura, I. Kushiro, Compositional relations of coexisting orthopyroxene, pigeonite and augite in a tholeiitic andesite from Hakone volcano, Contrib. Mineral. Petrol. 26 (1970) 265–275.
[84] B. Lothenbach, F. Winnefeld, Thermodynamic modelling of the hydration of Portland cement, Cem. Concr. Res. 36 (2006) 209–226.
[85] T. Matschei, B. Lothenbach, F.P. Glasser, Thermodynamic properties of Portland cement hydrates in the system $CaO–Al_2O_3–SiO_2–CaSO_4–CaCO_3–H_2O$, Cem. Concr. Res. 37 (2007) 1379–1410.
[86] B. Lothenbach, E. Wieland, A thermodynamic approach to the hydration of sulphate-resisting Portland cement, Waste Manag. 26 (2006) 706–719.
[87] B. Lothenbach, K. Scrivener, R.D. Hooton, Supplementary cementitious materials, Cem. Concr. Res. 41 (2011) 1244–1256.
[88] H. Taylor, Cement Chemistry, Thomas Telford, London, 1997.
[89] M. Wilke, G.M. Partzsch, R. Bernhardt, D. Lattard, Determination of the iron oxidation state in basaltic glasses using XANES at the K-edge, Chem. Geol. 213 (2004) 71–87.
[90] M.A. Marcus, A.J. Westphal, S.C. Fakra, Classification of Fe-bearing species from K-edge XANES data using two-parameter correlation plots, J. Synchrotron Radiat. 15 (2008) 463–468.
[91] P. Ghods, O. Isgor, G. McRae, G. Gu, Electrochemical investigation of chloride-induced depassivation of black steel rebar under simulated service conditions, Corros. Sci. 52 (2010) 1649–1659.
[92] G. Liu, Y. Zhang, Z. Ni, R. Huang, Corrosion behavior of steel submitted to chloride and sulphate ions in simulated concrete pore solution, Constr. Build. Mater. 115 (2016) 1–5.
[93] P.K. Mehta, P.J. Monteiro, Concrete: Microstructure, Properties, and Materials, McGraw Hill Education, New York, 2006.
[94] M. Bouchar, P. Dillmann, D. Neff, New insights in the long-term atmospheric corrosion mechanisms of low alloy steel reinforcements of cultural heritage buildings, Mater. 10 (2017) 670.
[95] P. Dillmann, F. Mazaudier, S. Hœrlé, Advances in understanding atmospheric corrosion of iron. I. Rust characterisation of ancient ferrous artefacts exposed to indoor atmospheric corrosion, Corros. Sci., 46 (2004) 1401–1429.
[96] A. Gruskovnjak, B. Lothenbach, F. Winnefeld, B. Münch, R. Figi, S.-C. Ko, M. Adler, U. Mäder, Quantification of hydration phases in supersulfated cements: review and new approaches, Adv. Cem. Res. 23 (2011) 265–275.
[97] P. Nadarajah, Chemistry and Corrosion Mechanisms of Steels Embedded in High-density Slag Concrete for Storage of Used Nuclear Fuel, University of Toronto, Toronto, 2011.
[98] P. Scott, S. Critchley, F. Wilkinson, The chemistry and mineralogy of some granulated and pelletized blastfurnace slags, Mineral. Mag. 50 (1986) 141–147.
[99] U. Angst, B. Elsener, C.K. Larsen, Ø. Vennesland, Critical chloride content in reinforced concrete—a review, Cem. Concr. Res. 39 (2009) 1122–1138.
[100] D. Neff, S. Reguer, P. Dillmann, Analytical Techniques for the Study of Corrosion of Metallic Heritage Artefacts: From Micrometer to Nanometer Scales, Corrosion and Conservation of Cultural Heritage Metallic Artefacts, Elsevier, 2013, pp. 55–81.
[101] A.J. Westphal, S.C. Fakra, Z. Gainsforth, M.A. Marcus, R.C. Ogliore, A. L. Butterworth, Mixing fraction of inner solar system material in Comet 81P/Wild2, Astrophys. J. 694 (2009) 18–28.